2010

Transfer operator-based approach for domain of attraction computation and experimental data analysis

Kai Wang
Iowa State University

Transfer operator-based approach for domain of attraction computation and experimental data analysis

by

Kai Wang

A thesis submitted to the graduate faculty

in partial fulfillment of the requirements for the degree of

MASTER OF SCIENCE

Major: Electrical Engineering

Program of Study Committee:
Umesh Vaidya, Major Professor
Baskar Ganapathysubramanian
Hui Hu

Iowa State University

Ames, Iowa

2010

DEDICATION

I would like to dedicate this thesis to my parents without whose support I would not have been able to complete this work.

TABLE OF CONTENTS

LIST OF FIGURES

PART I

TRANSFER OPERATER-BASED APPROACH FOR DOMAIN OF ATTRACTION COMPUTATION

OVERVIEW

The problem of computation of domain of attraction (DA) is of great practical interest given the importance of the problem in various engineering and physical systems. Examples include DA computation in power systems, chemical process, aircraft control, biological systems, and ecology.

Most of the existing methods for the computation of DA are Lyapunov functions based and are restricted to DA computation of an equilibrium point or at best periodic solution. There exists no method for DA computation of complex steady state such as chaotic attractor or sets consisting of quasi-periodic motion. Such steady states are often exhibited by complex dynamical systems. Examples include biological systems and synchronized state of coupled oscillators. Existing methods for DA computation are either developed for polynomial vector fields or relies on the point-wise description of the Lyapunov functions that describes DA. However complex dynamics can often be described most efficiently on sets as opposed to on points.

In this part, we propose a transfer operator-based method for the computation of DA. This proposed approach is used for almost everywhere global stability verification of an attractor set in nonlinear dynamical system. The basic idea behind the transfer operator approach is to replace the finite dimensional nonlinear evolution of dynamical system with a linear, albeit infinite dimensional, evolution described by linear transfer operator. This linear transfer operator is called as Perron-Frobenius (P-F) and is used to propagate sets or measure supported on sets in the phase space. The finite dimensional approximation of the P-F operator can be obtained using set-oriented numerical techniques developed by Dellnitz and group.

We extend the application of P-F operator along with set-oriented numerical methods for

the computation of DA. We show that the iterative algorithm based on P-F operator is efficient to compute the DA for any nonlinear system since it can not only characterize the DA for the nonlinear system with equilibrium dynamics but also system with complex non-equilibrium dynamics.

CHAPTER 1. INTRODUCTION

This introduction is divided into three sections. Section 1.1 briefly introduces P-F operator. Section 1.2 describes the motivations for computation of DA. And section 1.3 offers a review of existing papers.

1.1 Preliminaries

In this section, we present an introduction of P-F operator. This helps the reader to get an intuitive understanding of P-F operator before we define it strictly.

For a dynamical system, one can associate two different linear operators, called Koopman operator and P-F operator. While the dynamical system describes the evolution of an initial condition, the P-F operator describes the evolution of uncertainty in initial conditions. Set oriented numerical methods have recently been used to approximate the infinite dimensional P-F operator using their finite dimension counterpart [1]. In addition, the spectral analysis of the P-F operator gives a description of the asymptotic dynamics of nonlinear dynamical systems. In particular, the eigenfunction with eigenvalue 1 characterizes the invariant set capturing the long term asymptotic behavior of the system. Spectrum of the P-F operator on the unit circle has the information about the cyclic behavior of the system.

1.2 Motivations

In this section, we present the motivations for computation of DA of a nonlinear system.

When the origin $x = 0$ is asymptotically stable, we are often interested in determining how far from the origin the trajectory can be and still converge to the origin as t approaches ∞. This gives rise to the definition of the region of attraction (also called region of asymptotic

stability, domain of attraction, or basin) [2]. In this thesis, we use the terminology domain of attraction (DA).

For a linear system, the fact that an equilibrium point is locally asymptotically stable guarantees that an asymptotically stable behavior of the system around the equilibrium point. However, this is not true for nonlinear system. As for a nonlinear system, the locally asymptotic stability merely ensures that there exists a neighborhood of the equilibrium point such that all trajectories of the system converge to the equilibrium point for any initial condition in the neighborhood. Accordingly, a further investigation on the extension of the neighborhood is necessary in order to find a correct initialization of the system. Meanwhile, this is a problem of fundamental importance to be used in real plants where an incorrect initialization of the system may result in erroneous output[3]. For example, this problem is critical for those expensive and/or dangerous plants such as aircrafts, nuclear reactors, chemical plants, etc..., where unstable behaviors are not acceptable for disastrous consequences to which they could lead. Besides, the computation of DA is an important tool in controller design since perturbations from the equilibrium point within the DA are guaranteed to stay in it and converge to the equilibrium point.

It is well known that the DA of an equilibrium point is a complicated set and there exists no tractable analytic method to characterize the DA in the most cases. Recently, various numerical methods are proposed to estimate the DA for nonlinear systems.

1.3 Literature Review

In this section, we review existing literatures regarding estimation of DA. Most of the existing methods for computation of DA are Lyapunov functions based. Specifically, given a Lyapunov function for the equilibrium point, any Lyapunov function level set included in the region where the time derivative of Lyapunov function is negative is guaranteed to belong to the DA.

In [4], the paper deals with the problem of the estimation of regions of asymptotic stability for continuous, autonomous, nonlinear systems. Above all, a comprehensive survey of the

existing methods such as Lyapunov methods including Zubov method, La Salle method, and non-Lyapunov methods are provided. In addition, a "trajectory reversing method" allowing the DA estimation with the support of suitable topological considerations is proposed. Finally, several examples show the efficiency of this method for low order (second and third) systems. However, all those methods surveyed in this paper and the "trajectory reversing method" itself are restricted to DA computation of an equilibrium point or at best a limit cycle.

Due to the recent development in polynomial optimization based on the sum of square relaxations [5], it is possible to search for polynomial Lyapunov functions for systems with polynomial or rational dynamics. In [6], the problem of computing bounds on the DA for systems with polynomial vector field is considered. A methodology utilizing information from simulations to generate Lyapunov function candidates satisfying necessary conditions for bilinear constraints is proposed. The suitable Lyapunov function candidates are solved by linear sum-of-squares optimization problems. Qualified candidates are utilized to compute provably invariant subsets of the DA and to initialize various bilinear search strategies for further optimization.

In [7], special emphasis is laid on elaborating the connections between modern results of real algebraic geometry and Lyapunov's stability theory, namely between the positive definite polynomials and the direct method of Lyapunov. The estimation problem can thereby be reduced to solve a sequence of low non-convexity-rank bilinear matrix inequalities (BMI) optimization problems.

In [8], the author presents using bilinear sum of squares programming for enlarging a provable region of attraction of polynomial systems using polynomial functions. In order to keep the number of decision variables low, the author presents the use of composite Lyapunov functions. In addition, the author presents a method to find the outer bounds of attractive invariant set for polynomial system.

In [9], the asymptotically stable equilibrium points of polynomial systems have been investigated. A new algorithm for the computation of a subset of the DA based on a quadratic Lyapunov function has been presented.

From above, we know all methods presented in these papers can only be used to estimate the DA for the polynomial system. However, most real systems are non-polynomial systems, for example, pendulums, chemical reactors, and systems with saturations. Therefore, a method to determine the DA for non-polynomial systems is critical. In [10], a strategy for estimating the DA for non-polynomial systems via Lyapunov functions is proposed. Specifically, the author provides a strategy to estimate the DA of equilibrium points for non-polynomial systems via Lyapunov functions and Linear Matrix Inequality (LMI), based on the use of Taylor expansions and the parameterization of their remainders inside a convex polytopes. Furthermore, the author has offered conditions for non-conservative in case of fixed Lyapunov functions which are essential in order to obtain less conservative estimates in the case of variable Lyapunov functions.

In short, there exists no method for DA computation of complex steady state such as chaotic attractor or sets consisting of quasi-periodic motion. For example, biological systems show such steady states. Besides, we know existing methods for DA computation are either developed for polynomial vector fields or rely on the point-wise description of the Lyapunov functions that describes DA. However complex dynamics can often be described most efficiently on sets as opposed to on points.

CHAPTER 2. TRANSFER OPERATOR APPROACH FOR COMPUTING DOMAIN OF ATTRACTION

In this chapter, we extend the application of P-F operator along with set-oriented numerical methods for the computation of DA. The advantage of the proposed method over existing approaches is that it can be used for DA computation of general attractor set with the only requirement that the system mapping is differentiable function of the states.

The organization of the chapter is as follows. In section 2.1, we summarize the results on the application of transfer operator for global almost everywhere stability verification. The set-oriented numerical method for the finite dimensional approximation of the linear transfer operator are discussed in section 2.2. Our main result on the iterative approach for the computation of DA based on the finite dimensional approximation of the P-F operator is presented in section 2.3. In section 2.4, simulations for different systems are presented.

2.1 Lyapunov Measure for Stability

Definition 1 (Markov operator)**.** *Let $(X, \mathcal{A}, \mu)$ be a measure space. Any linear operator $P : L^1 \to L^1$ satisfying*

1. $Pf \geq 0 \quad$ *for* $f \geq 0, f \in L^1$
2. $\|Pf\| = \|f\| \quad$ *for* $f \geq 0, f \in L^1$

is called the Markov operator.

Definition 2 (Invariant measure)**.** *Invariant measure is a measure $\mu \in \mu(X)$ that satisfies*

$$\mu(A) = \int_X p(x, A) d\mu(x)$$

for all $A \in \mathcal{B}(X)$.

Definition 3 (Fixed point)**.** *If* P *is a Markov operator and, for some* $f \in L^1, Pf = f$*, then* f *is called a* ***fixed point*** *of* P.

Definition 4 (Measurable transformation)**.** *Let* $(X, \mathcal{A}, \mu)$ *be a measure space. A transformation* $S : X \to X$ *is* ***measurable*** *if*

$$S^{-1}(A) \in \mathcal{A} \quad \textit{for all } A \in \mathcal{A}.$$

Definition 5 (Nonsingular transformation)**.** *A measurable transformation* $S : X \to X$ *is measurable on a measurable space* $(X, \mathcal{A}, \mu)$ *is* ***nonsingular*** *if* $\mu(S^{-1}(A)) = 0$ *for all* $A \in \mathcal{A}$ *such that* $\mu(A) = 0$.

In this section, a discrete-time dynamical system with an attractor set $\mathcal{A}$ described by following equation

$$x_{n+1} = T(x_n) \tag{2.1}$$

where $x_n \in X \subset \mathbb{R}^N$ a compact set is considered. The mapping $T : X \to X$ is assumed to be differentiable and nonsingular.

$\mathcal{B}(X)$ denotes the Borel σ-algebra on X and $\mathcal{M}(X)$ is the vector space of real valued measure on X. The attractor set $\mathcal{A}$ for the dynamical system T is defined as follows:

Definition 6 (Attractor)**.** *A set* $\mathcal{A} \subset X$ *is said to be* T *invariant if* $T(\mathcal{A}) = \mathcal{A}$*. A closed* T *invariant set* $\mathcal{A}$ *is said to be attractor set if there exists a neighborhood* $V \subset X$ *of* $\mathcal{A}$ *such that* $\omega(x) \subset \mathcal{A}$ *for all* $x \in V$ *and there exists no strictly smaller set* $\mathcal{A}' \subset \mathcal{A}$ *that satisfies the above property.* V *is called the local neighborhood of* $\mathcal{A}$ *and* $\omega(x)$ *is the* ω*-limit set of* x.

Remark 7. *The important point of above definition is that it does not require the local stability (in the sense of Lyapunov) of the invariant set* A *and hence allows for a broad class of attractor sets [11].*

In [11], transfer operator-based framework was introduced to verify weaker notion of almost everywhere stability of an attractor set and defined as follows:

Definition 8 (Almost everywhere stability)**.** *The attractor set $\mathcal{A}$ for the dynamical system $T : X \to X$ is said to be almost everywhere stable with respect to finite non-negative measure $m \in \mathcal{M}(\mathcal{A}^c)$ if*

$$m\{x \in \mathcal{A}^c : \omega(x) \not\subseteq \mathcal{A}\} = 0$$

where $\omega(x)$ is ω-limit set of x.

The fundamental object of interest in the proposed transfer operator framework is the so-called linear Perron-Frobenius (P-F) operator. The linear P-F operator associated with the dynamical system T propagates uncertainty in the phase space and acts on the space of measures. The P-F operator is defined as follows:

Definition 9 (Perron-Frobenius operator)**.** *The linear P-F operator associated with dynamical system $T : X \to X$ is denoted by $\mathbb{P} : \mathcal{M}(X) \to \mathcal{M}(X)$ and is defined as follows:*

$$[\mathbb{P}\mu](B) = \int_X \chi_B(T(x))d\mu(x) = \mu(T^{-1}(B))$$

where $\chi_B(x)$ is the indicator function of the set $B \subset X$ and $T^{-1}(B)$ is the inverse image of set B.

The almost everywhere stability of the attractor set $\mathcal{A}$ is studied using the restriction of the P-F operator on the attractor set $\mathcal{A}$ and the complement of the attractor set $\mathcal{A}^c$. The restriction of the P-F operator on $\mathcal{A}$ and $\mathcal{A}^c$ are denoted by $\mathbb{P}_0 : \mathcal{M}(\mathcal{A}) \to \mathcal{M}(\mathcal{A})$ and $\mathbb{P}_1 : \mathcal{M}(\mathcal{A}^c) \to \mathcal{M}(\mathcal{A}^c)$ respectively and are defined as follows:

$$[\mathbb{P}_0\mu_0](B_0) = \int_{\mathcal{A}} \chi_{B_0}(T(x))d\mu_0(x)$$

$$[\mathbb{P}_1\mu_1](B_1) = \int_{\mathcal{A}^c} \chi_{B_1}(T(x))d\mu_1(x) = \mu_1(T^{-1}(B_1) \cap \mathcal{A}^c)$$

where $\mu_0 \in \mathcal{M}(\mathcal{A})$, $\mu_1 \in \mathcal{M}(\mathcal{A}^c)$, $B_0 \in \mathcal{B}(\mathcal{A})$, and $B_1 \in \mathcal{A}^c$. These restriction of P-F operators are used to define *Lyapunov measure*, which is used to verify global almost everywhere stability of an attractor set $\mathcal{A}$. In next section, we briefly summarize the main results from [11] on the almost everywhere stability verification using Lyapunov measure.

In [11], Lyapunov measure and Lyapunov measure equation were introduced for almost everywhere stability verification of an attractor set $\mathcal{A}$. The Lyapunov measure is defined as follows:

Definition 10 (Lyapunov measure)**.** *Let $U(\epsilon)$ be the ϵ neighborhood of the attractor set $\mathcal{A}$. The Lyapunov measure is defined as any non-negative measure $\bar{\mu} \in \mathcal{M}(\mathcal{A}^c)$ which is finite on $\mathcal{B}(X \setminus U(\epsilon))$ and satisfies following inequality*

$$[\mathbb{P}_1 \bar{\mu}](B) < \alpha \bar{\mu}(B) \tag{2.2}$$

for all set $B \in \mathcal{B}(X \setminus U(\epsilon))$ and for every $\epsilon > 0$. The $\alpha \leq 1$ is some constant.

The following theorem providing sufficient condition for almost everywhere stability of the attractor set $\mathcal{A}$ in terms of the existence of Lyapunov measure is proved in [11].

Theorem 11. *Suppose there exists a Lyapunov measure $\bar{\mu}$ with $\alpha = 1$, then the attractor set $\mathcal{A}$ is almost everywhere stable with respect to any finite measure m that is equivalent to $\bar{\mu}$.*

In the stability theory of dynamical system, we are particularly interested in the case where the measure $m \in \mathcal{M}(\mathcal{A}^c)$ is Lebesgue measure or absolutely continuous with respect to Lebesgue.

Remark 12. *If $\bar{\mu}$ is equivalent to Lebesgue measure, then the above theorem provides sufficient condition for global almost everywhere stability of the attractor set $\mathcal{A}$ with respect to Lebesgue measure.*

In the problem of DA computation, the set $\mathcal{A}$ will not be globally a.e. stable. Hence, it is of particular interest to provide conditions for the stability of the attractor set $\mathcal{A}$ with respect to initial condition starting from some particular set in X. Towards this we have the following theorem from [12] involving *Lyapunov measure equation*.

Theorem 13. *Let $m_B \in \mathcal{M}(\mathcal{A}^c)$ be the Lebesgue measure supported on set $B \subset X \setminus U(\epsilon)$. If there exists a non-negative measure $\bar{\mu} \in \mathcal{M}(\mathcal{A}^c)$ which is finite on $\mathcal{M}(X \setminus U(\epsilon))$ for any given $\epsilon > 0$ and satisfies following Lyapunov measure equation*

$$[\mathbb{P}_1 \bar{\mu}](D) - \bar{\mu}(D) = -m_B(D)$$

for all set $D \subset X \backslash U(\epsilon)$, then almost every (with respect to Lebesgue measure) initial conditions from the set B lies in the DA of the attractor set $\mathcal{A}$.

2.2 Finite Dimension Approximation

In this section we describe the set oriented numerical methods, developed by Dellnitz and group [1], for the finite dimensional approximation of the P-F operator. This finite dimensional approximation of the P-F operator is used for the computation of the Lyapunov measure in [13]. In this paper, we propose their application for the computation of DA. In order to obtain a finite-dimensional (discrete) approximation of the continuous P-F operator, one considers a finite partition of the phase space X, denoted as

$$X_L \doteq \{D_1, \cdots, D_L\}, \tag{2.3}$$

where $\cup_j D_j = X$. These partitions can be constructed by taking quantization for states in X. Instead of a Borel σ-algebra, consider now a σ-algebra of the all possible subsets of X_L. A real-valued measure μ_j is defined by ascribing to each element D_j a real number. Thus, one identifies the associated measure space with a finite-dimensional real vector space $\mathbb{R}^L$. In particular for $\mu = (\mu_1, ..., \mu_L) \in \mathbb{R}^L$ define a measure on X as

$$d\mu(x) = \sum_{i=1}^{L} \mu_i \kappa_i(x) \frac{dm(x)}{m(D_i)} \tag{2.4}$$

where m is the Lebesgue measure and κ_i denotes the indicator function with support on set D_i.

The discrete P-F approximation arises as a matrix on this "measure space" $\mathbb{R}^L$ and is given by

$$P_{ij} = \frac{m(T^{-1}(D_j) \cap D_i)}{m(D_i)}, \tag{2.5}$$

m being the Lebesgue measure. The resulting matrix is non-negative and because $T : D_i \to X$, $\sum_{j=1}^{L} P_{ij} = 1$ i.e., P is a Markov or a row-stochastic matrix. Computationally, several short-term trajectories are used to compute the individual entries P_{ij} . The mapping T is used to transport M initial conditions chosen to be uniformly distributed within a set D_i . The entry

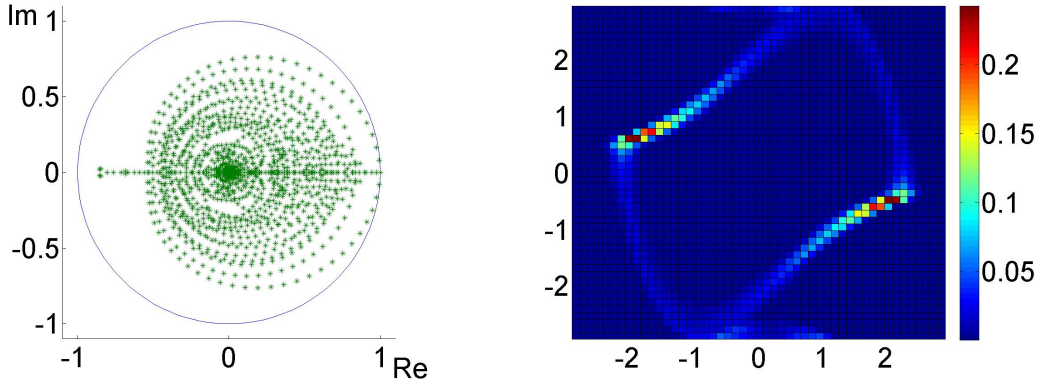

(a) Eigenvalues (b) invariant measure

Figure 2.1 Eigenvalues and the invariant measure of the discretized P-F matrix for the Van der Pol oscillator for $\epsilon = 1$

P_{ij} is then approximated by the fraction of initial conditions that are in the box D_j after one iterate of the mapping.

The finite-dimensional Markov matrix P is used to numerically study the approximate asymptotic dynamics of the Dynamical system T [1, 14].

In particular, suppose $\mu \geq 0$ is an invariant probability measure (vector), i.e.,

$$\mu P = 1 \cdot \mu, \tag{2.6}$$

such that $\sum \mu_i = 1$, then the support of μ gives the approximation of the attractor and $\mu_i = \mu(D_i)$ gives the "weight" of the component D_i in attractor A [15]. The dynamically relevant "almost invariant sets" are associated with the eigenmeasures with eigenvalues close to 1. And the cyclic behavior within an attractor can be extracted by considering the complex unitary spectrum of the Markov chain.

As an example, Figure 2.1 depicts the eigenvalues of the P-F operator and the invariant measure for the Van der Pol oscillator example $\dot{x}_1 = x_2 \quad \text{and} \quad \dot{x}_2 = -x_1 + \epsilon(1 - x_1^2)x_2$, where ϵ is a scalar parameter.

We begin by presenting a decomposition result for the approximation P corresponding to a finite partition. It is assumed that an approximation μ_0, to the invariant measure μ of an

attractor set $A \subset X$, has been computed by evaluating a fixed-point the matrix P. An indexing is chosen such that the two non-empty complementary partitions

$$\mathcal{X}_0 = \{D_1, ..., D_K\}, \quad \mathcal{X}_1 = \{D_{K+1}, ..., D_L\} \tag{2.7}$$

with domains $X_0 = \cup_{j=1}^{K} D_j$ and $X_1 = \cup_{j=K+1}^{L} D_j$ distinguish the approximation of the attractor set from its complement set respectively. In particular, $A \subset X_0$, μ_0 is supported and non-zero on $\mathcal{X}_0$, and one is interested in stability w.r.t the initial conditions in the complement X_1. For an attractor A with an invariant measure defined w.r.t a neighborhood $U \supset A$, such sets exist for a sufficiently fine partition such that $A \subset X_0 \subset U$. The following Lemma summarizes the matrix decomposition result.

Lemma 14. *Let P denote the Markov matrix for the mapping T in Eq. (2.1) defined w.r.t the finite partition $\mathcal{X}$ in Eq. (2.3). Let $M \cong \mathbb{R}^L$ denote the associated measure space and μ denote a given invariant vector of P. Suppose $\mathcal{X}_0$ and $\mathcal{X}_1$ are the two* non-empty *components as in Eq. (2.7) defined w.r.t μ such that $\mu > 0$ on $\mathcal{X}_0$; $\mu_i > 0$ iff $D_i \in \mathcal{X}_0$. Let $M_0 \cong \mathbb{R}^K$ and $M_1 \cong \mathbb{R}^{L-K}$ be the measure spaces associated with $\mathcal{X}_0$ and $\mathcal{X}_1$ respectively. Then for the splitting $M = M_0 \oplus M_1$, the P matrix has a lower triangular representation*

$$P = \begin{bmatrix} P_0 & 0 \\ \times & P_1 \end{bmatrix} \tag{2.8}$$

where $P_0 : M_0 \to M_0$ is the Markov matrix with row sum equal to one and $P_1 : M_1 \to M_1$ is the sub-Markov matrix with row sum less than or equal to one.

Proof. Use the splitting $M = M_0 \oplus M_1$ to express the invariant vector $\mu = [\mu^0, \mu^1]$ where, $\mu_0 \in M_0$ and $\mu_1 \in M_1$. By construction, $\mu^0 > 0$ for all entries and $\mu^1 = 0$. Again, use the splitting to write

$$P = \begin{bmatrix} P_0 & 0 \\ \times & P_1 \end{bmatrix} \tag{2.9}$$

In order to prove the result, note that P is non-negative matrix such that

$$[\mu^0, 0] = \mu P = [\mu^0 P_0, \mu^0 P_2].$$

Since, $\mu^0 > 0$ so $P_2 = 0$. □

We remark that this decomposition result does not explicitly require either the existence of the set U or any property $A \subset X_0 \subset U$ regarding the partition $\mathcal{X}_0$. These two however ensure that a) $\mathcal{X}_0$ and $\mathcal{X}_1$ are non-empty and b) the invariant vector is a good approximation of the invariant measure and hence the underlying attractor.

This finite dimensional approximation of the P-F operator and the above described decomposition of the P-F operator are used for the computation of Lyapunov measure. While the existence of infinite dimensional Lyapunov measure implies almost everywhere stability of the attractor set, the existence of the finite dimensional Lyapunov measure implies a weaker notion of stability referred to as *coarse stability* [11].

The coarse stability of the attractor set A is defined as follows:

Definition 15 (Coarse Stability)**.** *Consider an attractor $A \subset X_0$ together with a finite partition $\mathcal{X}_1$ of the complement set $X_1 = X \backslash X_0$. A is said to be* **coarse stable** *w.r.t the initial conditions in X_1 if for an attractor set $B \subset U \subset X_1$, there exists no sub-partition $\mathcal{S} = \{D_{s_1}, D_{s_2}, \ldots, D_{s_l}\}$ in $\mathcal{X}_1$ with domain $S = \cup_{k=1}^{l} D_{s_k}$ such that $B \subset S \subset U$ and $T(S) \subseteq S$.*

For *typical* partitions, coarse stability means stability modulo attractor set B with DA U smaller than the size of cells within the partition. In the infinite-dimensional limit, where the cell size (measure) goes to zero, one obtains stability modulo attractor sets with measure 0 DA, i.e., a.e. stability.

Theorem 16. *Assume the notation of the Lemma 14. In particular, A is an attractor set in $X_0 \subset X$ with approximate invariant measure supported on the finite partition $\mathcal{X}_0$ of X_0. $\mathbb{P}_1$ is the sub-Markov operator on $\mathcal{M}(A^c)$. P_1 is its finite-dimensional sub-Markov matrix approximation obtained with respect to the partition $\mathcal{X}_1$ of the complement set $X_1 = X \setminus X_0$. For this*

1. *Suppose a Lyapunov measure $\bar{\mu}$ exists such that $\mathbb{P}_1\bar{\mu}(B) < \bar{\mu}(B)$ for all $B \subset \mathcal{B}(X_1)$, and additionally $\bar{\mu} \approx m$, the Lebesgue measure. Then the finite-dimensional approximation P_1 is transient (i.e., $\lim_{n\to\infty} P_1^n = 0$).*

2. *Suppose P_1 is transient then A is coarse stable w.r.t the initial conditions in X_1.*

In summary, a.e. stability implies P_1 is transient, while one can only conclude a weaker coarse stability given transience of P_1.

2.3 Domain of Attraction Computation

In this section, we present a numerical scheme based on finite dimensional approximation of P-F operator for the computation of DA. In [13], we have employed the finite dimensional approximation of P-F operator for the computation of Lyapunov measure, used for verifying global almost everywhere stability of the attractor set. There is one key difference between the numerical scheme adopted for the computation of Lyapunov measure and for the computation of DA. The difference is that in the computation of Lyapunov measure we discretized the entire phase space for constructing the finite dimensional approximation of the P-F operator. *However for the computation of DA, we employ an iterative scheme whereby at each step of the iteration we construct the approximation of the P-F operator only on the small portion of the phase space X.* This iterative feature of the proposed algorithm greatly helps in reducing the computational burden associated with the approximation of the P-F operator. The iterative algorithm for the computation of DA can be explained formally with the help of Figure 2.2 as follows:

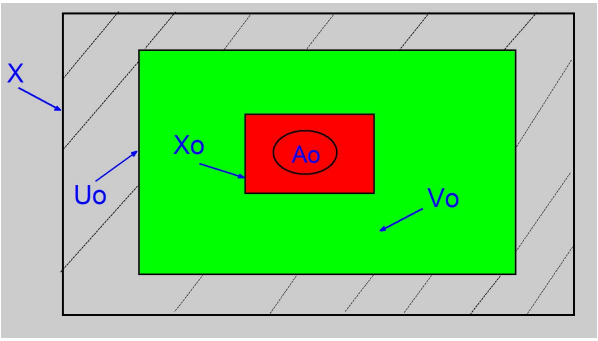

Figure 2.2 Scheme for computation of domain of attraction

Step 1: First we identify the attractor set A_0 whose DA needs to be computed. The attractor set A_0 along with its neighborhood $X_0 \supset A_0$ is marked as red in Fig. 2.2.

Step 2: We start with the initial domain $U_0 \supset X_0 \supset A_0$ and let $V_0 = U_0 \setminus X_0$. V_0 marked as green in Fig. 2.2. The objective is to determine the set of initial conditions in V_0 that lies in the DA of the attractor set A_0. We assume that the domain V_0 does not contain any attractor set. This assumption is justified because U_0 is the initial domain of investigation and can always be chosen small enough to ensure non-existence of attractor set other than A_0. However set of initial conditions in V_0 might lie in the DA of attractor set A_0.

Step 3: The domain outside the neighborhood U_0 is denoted by $\tilde{A}_0$ and marked with hashed in Fig. 2.2.

Step 4: With the above labeling, we write the state space $X = U_0 \cup \tilde{A}_0$, where $U_0 = X_0 \cup V_0$. We consider following partition of the state space $\mathcal{X} = \{D_1, \ldots, D_{L_0}, D_{L_0+1}, \ldots, D_{N_0}, D_{N_0+1}\}$ such that $V_0 = \cup_{j=1}^{L_0} D_j$, $X_0 = \cup_{i=L_0+1}^{N_0} D_i$, and $\tilde{A}_0 = D_{N_0+1}$. Note that the entire region $\tilde{A}_0$ is represented by the single cell D_{N_0+1} from the partition $\mathcal{X}$ and hence the finite dimensional approximation of the P-F operator is essentially constructed on the domain U_0.

Step 5: The domain $\tilde{A}_0$ is coarsely resolved using the single cell D_{L_0+1} and hence the finite dimension approximation of the P-F operator restricted to $\tilde{A}_0$ is a one-by-one matrix. Since the domain of investigation at this stage is V_0, without loss of generality we can assume that the 1×1 matrix restricted to $\tilde{A}_0$ is Markov. We denote this matrix by $P_{\tilde{A}_0}$ with the form $P_{\tilde{A}_0} = [1]$.

Step 6: The P-F operator restricted to the attractor set A_0 is Markov and its finite dimensional approximation is a $(N_0 - L_0) \times (N_0 - L_0)$ matrix, denoted by P_{A_0}.

Step 7: The finite dimensional approximation for the restriction of P-F operator to the domain V_0 is a $L_0 \times L_0$ sub-Markov matrix and is denoted by P_{V_0}.

Step 8: Let $P_0 = diag(P_{A_0}, P_{\tilde{A}_0})$, which is a Markov matrix from step 5 and 6. The finite dimensional approximation of the P-F operator on the partition $\mathcal{X}$ can hence be written as

$$P = \begin{pmatrix} P_0 & 0 \\ R_{V_0} & P_{V_0} \end{pmatrix} \tag{2.10}$$

Step 9: The sub-Markov matrix P_{V_0} is transient because the domain V_0 does not contain any attractor set and hence the matrix $(I - P_{V_0})^{-1}$ is well defined. There are three possibilities

for the set of initial conditions in the domain V_0. They are, the set of initial conditions in V_0 lies

a) in the DA of attractor set A_0. We denoted this set of initial conditions by $\mathcal{O}_{A_0}$;

b) in the DA of the attractor set which lies in $\tilde{A}_0$. We denote this set by $\mathcal{O}_{\tilde{A}_0}$;

c) on the "boundary" of the two attractor sets A_0 and $\tilde{A}_0$. We denote this set of initial conditions by $\mathcal{O}_{A_0||\tilde{A}_0}$.

Step 10: For computing the DA, we need to determine the set $\mathcal{O}_{A_0}$. The characterization of the sets $\mathcal{O}_{A_0}$, $\mathcal{O}_{\tilde{A}_0}$, and $\mathcal{O}_{A_0||\tilde{A}_0}$ can be provided using results from the theory of Markov chain (Theorem 18).

Step 11: Once $\mathcal{O}_{A_0}$, $\mathcal{O}_{\tilde{A}_0}$, and $\mathcal{O}_{A_0||\tilde{A}_0}$ are identified, we proceed to the next step of the iteration by redefining the new attractor set A_1 and its neighborhood $X_1 := X_0 \cup \mathcal{O}_{A_0}$. A new domain U_1 for investigation of DA of A_1 is chosen to include part of $\tilde{A}_0$ such that $\tilde{A}_1 \subset \tilde{A}_0$ and $X = U_1 \cup \tilde{A}_1 = (X_1 \cup V_1) \cup \tilde{A}_1$. The choice of U_1 is based on the location of the set $\mathcal{O}_{A_0||\tilde{A}_0}$.

We now proceed to provide characterization for the above three sets described in step 9 using Markov matrix P. Let the attractor set be A and our goal is to find the set $\mathcal{O}_A$. Without loss of generality we can identify all the cells containing the attractor set A along with its neighborhood with single cell in the partition $\mathcal{X}$ and the associated finite dimensional P-F matrix as 1×1 unity matrix. Hence the finite dimensional approximation of the P-F operator P at any step of the iteration can be written as

$$P = \begin{pmatrix} I & 0 \\ R_V & P_V \end{pmatrix} \tag{2.11}$$

where I is a 2×2 identity matrix. The Markov matrix P is now in the so called *canonical form* where the two absorbing states corresponding to the two attractor sets A and $\tilde{A}$ and is represented by the 2×2 identity matrix I and the L transient states in V are represented by the sub-Markov matrix P_V. We now state following two standard results from Markov chain theory from [16], the results of these theorems are used to characterize $\mathcal{O}_A, \mathcal{O}_{\tilde{A}}$, and $\mathcal{O}_{A||\tilde{A}}$.

Theorem 17. *For the absorbing Markov matrix (2.11), the sub-Markov matrix P_V is transient*

(i.e., $\lim_{n\to\infty} P_V^n \to 0$*) and hence* $(I - P_V)^{-1}$ *is well defined.*

Theorem 18. *Let* $s_1, \ldots, s_L$ *denote the transient states and* s_A *and* $s_{\tilde{A}}$ *denote the states for the attractor set* A *and* $\tilde{A}$ *respectively in the Markov matrix* P*. Let* b_{iA} *and* $b_{i\tilde{A}}$ *be the probability that the Markov chain* P *be observed in the set* s_A *and* $s_{\tilde{A}}$ *starting from the transient set* s_i *respectively. Let* B *be the matrix with entries* b_{iA} *and* $b_{i\tilde{A}}$ *for* $i = 1 \ldots L$*. Then* B *is a* $L \times 2$ *matrix, and is given by*

$$B = Q_V R_V \tag{2.12}$$

where $Q_V = (I - P_V)^{-1}$*.*

Proof. Let $[P_V]_{ik}^n$ denotes the $\{i, k\}$ entry of the matrix P_V^n. We have

$$\begin{aligned} [B]_{ij} &= \sum_{n=0}^{\infty}\sum_{k=1}^{L}[P_V]_{ik}^n[R_V]_{kj} = \sum_{k=1}^{L}\sum_{n=0}^{\infty}[P_V]_{ik}^n[R_V]_{kj} \\ &= \sum_{k=1}^{L}[Q_V]_{ik}[R_V]_{kj} = [Q_V R_V]_{ij} \end{aligned} \tag{2.13}$$

□

The matrix B can be used to characterize the three sets of interest. In particular the cell D_i that lies in the DA of the attractor set A corresponds to the states s_i for which $b_{iA} = 1$. Hence,

- $\mathcal{O}_A = \{x \in D_i : \quad b_{iA} = 1 \quad \text{or} \quad b_{i\tilde{A}} = 0\}$;
- $\mathcal{O}_{\tilde{A}} = \{x \in D_i : \quad b_{i\tilde{A}} = 1 \quad \text{or} \quad b_{iA} = 0\}$;
- $\mathcal{O}_{A||\tilde{A}} = \{x \in D_i : \quad 0 < b_{i\tilde{A}} < 1\}$.

2.3.1 Procedure for Constructing Markov Matrix from the Sub-Markov Matrix

Consider a domain $U \subset X$ and a partition $\mathcal{X}$ of U consisting of N cells. Let $P \in \mathbb{R}^{N\times N}$ be the finite dimensional approximation of the P-F operator constructed on the partition $\mathcal{X}$. If no trajectory escapes U, then P is a stochastic Markov matrix. However if positive measure set of initial conditions escapes the domain U, then P is a sub-Markov matrix. We outline following

procedure to construct Markov matrix from the sub-Markov matrix. If P is sub-Markov, then define matrix $P_f := P$. The Markov matrix constructed from sub-Markov matrix P_f is a $(N+1) \times (N+1)$ matrix constructed as follows:

$$P = \begin{pmatrix} P_f & \mathbf{1} - S \\ \mathbf{0} & 1 \end{pmatrix} \tag{2.14}$$

where $P_f \in \mathbb{R}^{N \times N}$ is the sub-Markov matrix, $\mathbf{1} \in \mathbb{R}^{N \times 1}$ is a column vector of all ones, $S \in \mathbb{R}^{N \times 1}$ is a column vector and its entry $S_i = \sum_{j=1}^{N} (P_f)_{ij}$, and $\mathbf{0} \in \mathbb{R}^{1 \times N}$ is a row vector of all zeros. The $(N+1)^{th}$ state of P is associated with the attractor set $\tilde{A}$ lying outside the domain U.

2.3.2 Iterative Algorithm for Computation of DA

Step 1: Let j be the step of iteration and $j = 0$. Let A_j be the attractor set and V_j be the domain under investigation.

Step 2: Compute the finite dimensional approximation of the P-F operator: $P \in \mathbb{R}^{N_j \times N_j}$ on V_j.

Step 3: If P is a Markov matrix, then jump to step 4. Otherwise, construct $P \in \mathbb{R}^{(N_j+1) \times (N_j+1)}$ using the construction procedure outlined in subsection 2.3.1.

Step 4: Compute $B = (I - P_{V_j})^{-1} R_{V_j}$. Identify those states which are in DA of A_j using the results and discussion following Theorem 18.

Step 5:

- If DA exists for attractor set A_j, say $\mathcal{D}_j$, then enlarge the attractor set A_j to incorporate $\mathcal{D}_j$ for $(j+1)^{th}$ step, that is $A_{j+1} := A_j \cup \mathcal{D}_j$. Include the new domain V_{j+1} around A_{j+1} and redefine $j =: j + 1$. Jump to step 2.

- If DA for attractor set A_j does not exist, then jump to step 6.

Step 6: Stop the program.

2.4 Simulations for Domain of Attraction

In this section we describe various examples of two and three dimensional continuous and discrete-time systems consisting of polynomial and non-polynomial vector field. Examples also include systems with non-trivial attractor set (i.e. not equilibrium points). All computations are performed using MATLAB on a desktop PC. The MATLAB code written for DA computation is not optimized for the computation time.

2.4.1 Example for a 2 Dimensional Polynomial System

Example 1: Our first example is that of a polynomial vector field from [4] and is described by the following set of equations:

$$\begin{aligned} \dot{x}_1 &= -x_1 + 2x_1^2 x_2 \\ \dot{x}_2 &= -x_2 \end{aligned} \tag{2.15}$$

The system has origin as the unique stable equilibrium point. From the phase portrait plot we see that the second and the fourth quadrant are in DA of $x = 0$. The curve $x_1 x_2 = 1$ describes the boundary of actual DA in the first and third quadrant.

Fig. 2.3 shows the DA marked with red, and the boundary cells are marked with green for this system. The yellow curves in the second and the fourth quadrant satisfy $x_1 x_2 = 1$. The domain of investigation is chosen to be $[-2, 2] \times [-2, 2]$. The total simulation time for DA computation is equal to 8.5 seconds. The total simulation time is a function of many parameters such as number of cells used for finite dimensional approximation of P-F and number of points per cell used for the generation of P-F. All these parameters need to be optimized in order to improve the speed of DA computation.

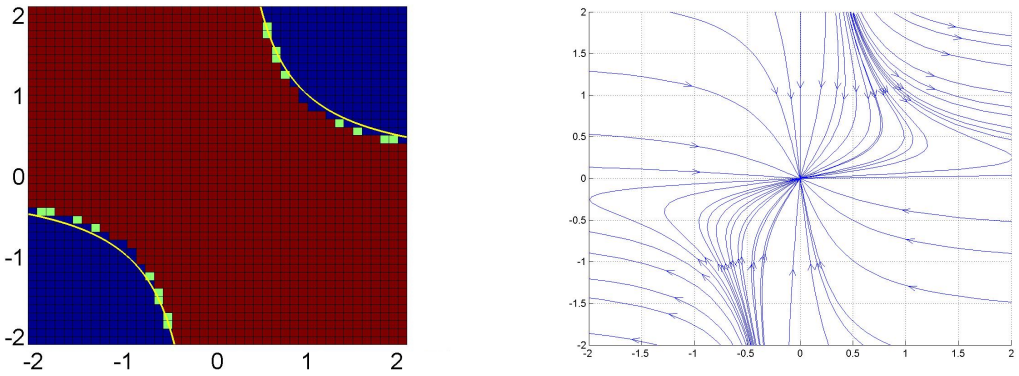

(a) DA (in red) and boundary cells (in green)

(b) Phase portrait

Figure 2.3 Domain of attraction and phase portrait for Example 1

2.4.2 Example for a 2 Dimensional Non-polynomial System

Example 2: Our second example from [10] is that of a non-polynomial vector field described by the following set of equations:

$$\begin{aligned} \dot{x}_1 &= -x_1 + x_2 + 0.5(e^{x_1} - 1) \\ \dot{x}_2 &= -x_1 - x_2 + x_1 x_2 + x_1 \cos x_1 \end{aligned} \tag{2.16}$$

The origin is a stable equilibrium point of the system. The total simulation time for the DA computation for this example is 23 seconds. Again DA is marked with red, and the boundary cells are marked with green in Fig. 2.4.

2.4.3 Example for a 3 Dimensional Polynomial System

Example 3: Our third example from [6] is that of a polynomial vector field described by the following set of equations:

$$\begin{aligned} \dot{x}_1 &= -x_1 + x_2 x_3^2 \\ \dot{x}_2 &= -x_2 + x_1 x_2 \\ \dot{x}_3 &= -x_3 \end{aligned} \tag{2.17}$$

The origin is the unique equilibrium point of this 3 dimensional system and it is a stable equilibrium point. We choose the domain of investigation for DA to be equal to $[-2.1, 2.1] \times$

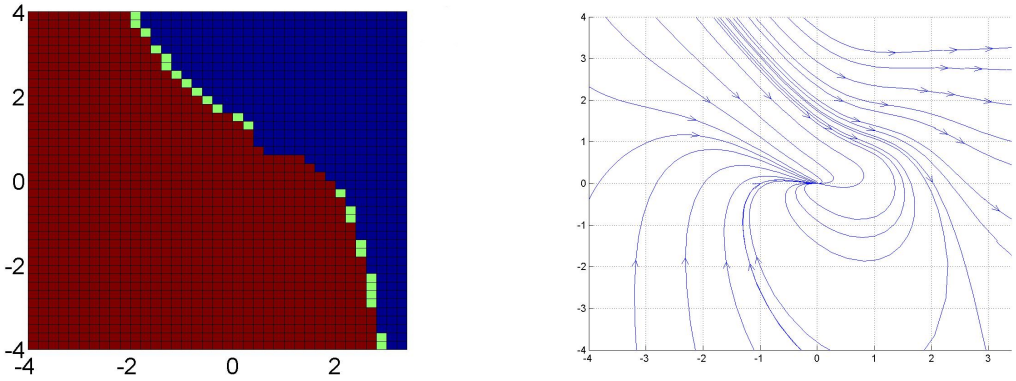

(a) DA (in red) and boundary cells (in green)

(b) Phase portrait

Figure 2.4 Domain of attraction and phase portrait for Example 2

$[-2.1, 2.1] \times [-2.1, 2.1]$. For better visualization we plot the DA from three different angles in Fig. 2.5 (a), (b), (c). The total simulation time for this example is 104 seconds.

2.4.4 Example for Henon Map

Example 4: Our fourth example is the Henon map described by the following set of equations:

$$\begin{aligned} x_{n+1} &= y_n + 1 - ax_n^2 \\ y_{n+1} &= bx_n \end{aligned} \tag{2.18}$$

where, $a = 1.4$ and $b = 0.3$ are two parameters. For those parameter values, Henon map is chaotic with nontrivial attractor set. Since the chaotic attractor is contained in $[-3, 3] \times [-1, 1]$, the initial domain for computation of DA in the first step of iteration should incorporate $[-3, 3] \times [-1, 1]$. The total simulation time for this example is 7.8 seconds.

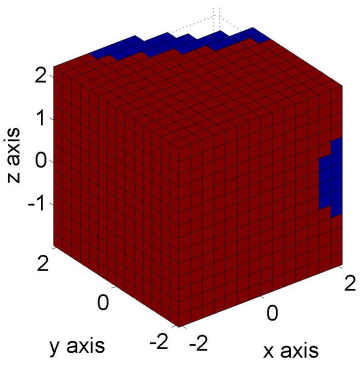

(a) DA (in red) and boundary cells (in blue)

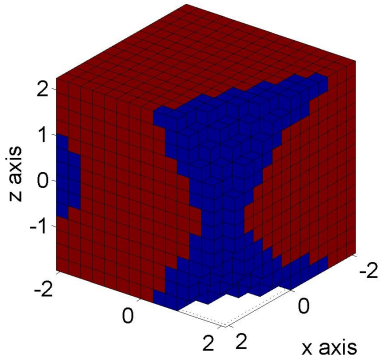

(b) DA (in red) and boundary cells (in blue)

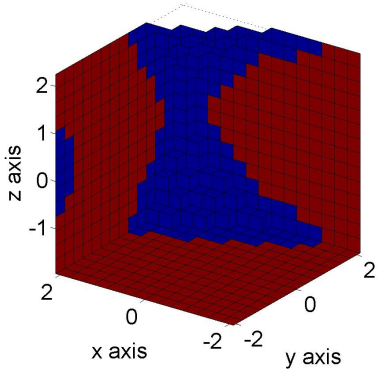

(c) DA (in red) and boundary cells (in blue)

Figure 2.5 Domain of attraction and boundary cells for Example 3

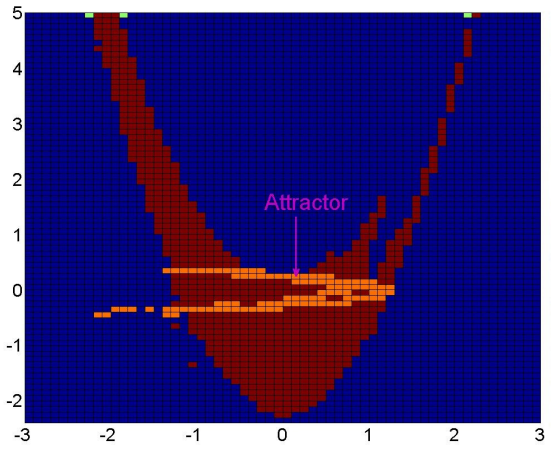

Figure 2.6 Domain of attraction (in red) and boundary cells (in green) for Example 4

2.4.5 Example for Chua's Equation

Example 5: Our fifth example [17] is the ODE equivalent of Chua's equation described by the following set of equations:

$$\begin{aligned} \dot{x} &= q_1 x - y + (p_1 - q_1)h(x) \\ \dot{y} &= q_2 x - z + (p_2 - q_2)h(x) \\ \dot{z} &= q_3 x + (p_3 - q_3)h(x) \end{aligned} \tag{2.19}$$

where, $h(x) = \frac{1}{2}(|x+1| - |x-1|)$, and the parameters $p_1 = 0.3625$, $p_2 = 1.063125$, $p_3 = 0.2765625$, $q_1 = -10.2875$, $q_2 = -1.2$, $q_3 = -2.71875$.

This system has a chaotic attractor plotted in Fig. 2.7. The phase space we investigate is $[-2.5, 2.5] \times [-2.5, 2.5] \times [-2.5, 2.5]$, and the total simulation time is 15 minutes. We plot the DA from three different angles in Fig. 2.8 (a), (b), (c).

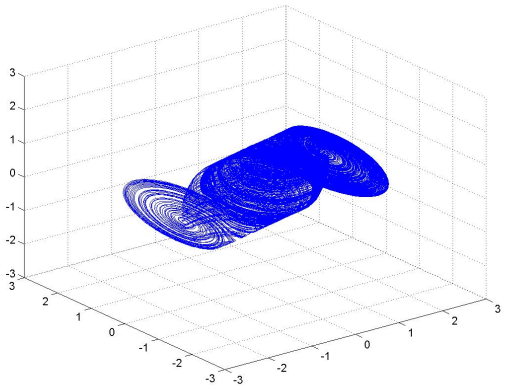

Figure 2.7 Attractor set for Example 5

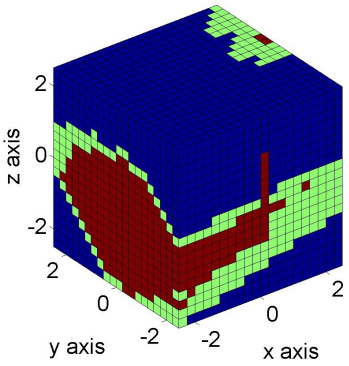

(a) DA (in red) and boundary cells (in green)

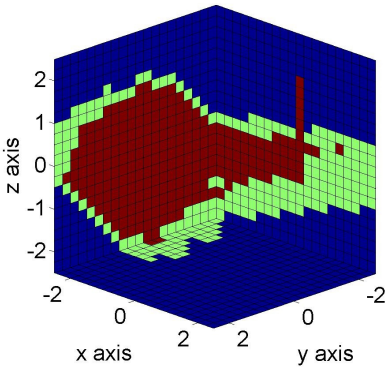

(b) DA (in red) and boundary cells (in green)

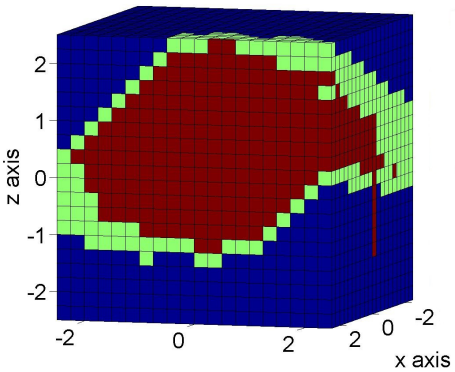

(c) DA (in red) and boundary cells (in green)

Figure 2.8 Domain of attraction and boundary cells for Example 5

CHAPTER 3. CONCLUSIONS AND FUTURE RESEARCH

3.1 Conclusions

In the past few years, existing methods of DA computation are Lyapunov function based. There is no method for DA computation of complex steady state such as chaotic attractor or sets consisting of quasi-periodic motion.

The transfer operator approach for computation of DA overcomes the shortcomings of almost all existing methods. An iterative algorithm for the computation of the DA based on the set-oriented numerical approaches used for finite dimensional approximation of linear transfer operator has been presented. Simulation results illustrate that the iterative algorithm can not only characterize the DA for the system with equilibrium dynamics but also system with complex non-equilibrium dynamics.

3.2 Future Research

Now, we can apply the P-F operator based iterative algorithm to any 2 dimensional or 3 dimensional system. This algorithm is efficient for 2 dimensional systems since in general computation time is less than 10 seconds. However, computation times for most of the 3 dimensional systems are larger than 10 minutes and thus it is not efficient enough in comparison to the computation efficiency for 2 dimension system. Thereby, further researches will focus on improving the efficiency of the iterative algorithm and applying the algorithm to higher dimensional nonlinear dynamical systems.

PART II

EXPERIMENTAL DATA ANALYSIS

OVERVIEW

Modern experiments and/or simulations in fluid flows generate a large amount of data containing valuable information that can be used to analyze the dynamics of turbulence. Nevertheless, it is not feasible to analyze the complex flow phenomena directly from raw time histories of the dynamics. In practice, people use modal decomposition technique to decompose the complex flow structures into modes to automatically extract, organize and classify the vortical structures (also called coherent structures). The vortical structures hold significant fraction of the total turbulent energy and affect numerous technologically momentous processes.

The objective of this part is to compare existing methods and develop novel approaches for experimental data analysis of the unsteady aerodynamics of the flapping wing microaerial-vehicle. These methods are developed for the purpose of identification of the beneficial dynamics and for the development of reduced order models for control design. In this part, Proper Orthogonal Decomposition (POD) method and spectral analysis method based on Perron-Frobenius (P-F) mode are utilized to analyze experimental data of flapping wings respectively.

We first employ POD method for the data analysis of the PIV measurements in the wakes of piezoelectric flapping wings. The basic idea behind POD based data analysis method is to decompose the time series snapshots of PIV measurements into high energy, POD, modes. The POD modes obtained from the PIV measurement data with different control inputs, such as flapping amplitude and flight speed, are compared to identify high energy modes that are invariant across the range of operating conditions. Similarly the modes that are responsible for maximum energy transfer between the control inputs and the desired output such as lift and thrust are identified.

The second method that we propose for the PIV measurements analysis is inspired from our recent work to develop a novel approach for the spectral analysis of the nonlinear flows. This new method is based on the spectral analysis of the linear transfer operator, the so called Koopman operator, associated with any nonlinear flows. The motivation for this work comes from the desire to perform frequency-based decomposition of the snapshot data as opposed to energy based decomposition in the POD method. While POD-based data analysis method captures all modes containing high energy, it ignores the low energy modes. These low energy modes might play an important role from the dynamics point of view and hence cannot be ignored. We perform the spectral analysis of the linear transfer, Perron-Frobenius (P-F) operator, which is dual to the Koopman operator to obtain the frequency based decomposition of the time series snapshot data. The basic idea behind this approach is to construct the finite dimensional approximation of the linear transfer (P-F) operator that best describes the time evolution of the snapshots data. The eigenvalues and eigenvectors of this transfer operator carry useful information about the system dynamics.

CHAPTER 4. INTRODUCTION

This introduction is divided into four sections. Section 4.1 briefly introduces the POD modes, Koopman operator and Koopman modes. Section 4.2 describes the motivations for experimental analysis of flapping wings. Section 4.3 offers a review of existing papers. Finally, section 4.4 introduces the experimental set up of flapping wings.

4.1 Preliminaries

4.1.1 Proper Orthogonal Decomposition Mode

The Proper Orthogonal Decomposition (POD), also called the Principal Component Analysis (PCA), or the Karhunen-Lo$'$eve (KL) decomposition, is a common technique to reduce a complicated flow behavior to a simpler one and to get the coherent structure of fluid flow.

Suppose we have a finite-dimension space $\mathbb{R}^n$ where n is equal to the number of grid points times the number of the flow variables, and we have a set of data given by $x(t) \in \mathbb{R}^n$, with $0 \leq t \leq T$. We try to seek a projection $P_r : \mathbb{R}^n \to \mathbb{R}^n$ of fixed rank r to minimize the total error, given by

$$\int_0^T \|x(t) - P_r x(t)\|^2 \, dt. \tag{4.1}$$

To this end, we introduce a $n \times n$ matrix

$$R = \int_0^T x(t)x(t)^* dt \tag{4.2}$$

where * denotes the matrix transpose.

The eigenvalues and eigenvector of R are given by

$$R\phi_k = \lambda_k \phi_k, \quad 0 \leq \lambda_n \leq \cdots \leq \lambda_1. \tag{4.3}$$

Since R is a symmetric and positive-semidefinite matrix, all eigenvalues λ_k are real and nonnegative, and the eigenvectors ϕ_k may be chosen to be orthogonal. The main result of POD is that the optimal subspace of dimension r is spanned by $\phi_1, \cdots, \phi_r$, and the optimal projection P_r is then given by

$$P_r = \sum_{k=1}^{r} \phi_k \phi_k^*. \tag{4.4}$$

The vectors $\phi_k, 1 \leq k \leq r$ are called POD modes [18].

Furthermore, the energy of projection is given by

$$\int_0^T \|P_r x(t)\|^2 \, dt = \sum_{k=1}^{r} \lambda_k \tag{4.5}$$

That is, λ_k denotes the kinetic energy of POD mode ϕ_k.

4.1.2 Koopman Operator and Koopman Mode

Definition 19 (Koopman operator)**.** *Let $(X, \mathcal{A}, \mu)$ be a measure space. If $S : X \to X$ is a nonsingular transformation, and $f \in L^\infty$. The operator $U : L^\infty \to L^\infty$ defined by*

$$Uf(x) = f(S(x)) \tag{4.6}$$

*is called the **Koopman operator** with respect to S [19].*

The Koopman operator, a infinite dimensional linear operator, has one important property that for every $f \in L^1$, $g \in L^\infty$, $\langle Pf, g \rangle = \langle f, Ug \rangle$ so that U is adjoint to the P-F operator P.

Let ϕ_j be the eigenfunction and λ_j be the eigenvalue of Koopman operator,

$$U\phi_j(x) = \lambda_j \phi_j(x) \tag{4.7}$$

Given a vector-valued observable $\mathbf{g}(\mathbf{x})$, we can expand $\mathbf{g}(\mathbf{x})$ in terms of these eigenfunctions as

$$\mathbf{g}(\mathbf{x}) = \sum_{\mathbf{j=1}}^{\infty} \phi_{\mathbf{j}}(\mathbf{x}) \mathbf{V_j} \tag{4.8}$$

where, $\mathbf{V_j}$ is called the **Koopman mode** [20].

4.2 Motivations for Experimental Data Analysis

4.2.1 Proper Orthogonal Decomposition Mode Analysis

Numerous studies have been conducted in recent years to investigate the flow pattern and vortex structures in the wakes of flapping wings. The experimental research in fluid flows generates a large amount of instantaneous data. As we know, POD method uses the spatial or temporal correlation matrix to compute the eigenfunction, POD mode, and thus decomposes the structures contained in snapshots from the energy point of view. Using POD method to analyze the experimental data of flapping wing provides an efficient way to identify high energy modes that remain invariant across range of operating conditions because POD method captures more kinetic energy than any other model reduction method given a number of POD modes.

4.2.2 Spectral Analysis

The motivation for spectral analysis of experimental data is to perform frequency-based decomposition of the snapshot data as opposed to energy based decomposition in the POD method. These low energy modes ignored in POD modes might play an important role from the dynamics point of view. For example, acoustic waves play a critical role in a fluid flow where acoustic resonances occur even though hydrodynamic pressure fluctuations have larger energy than acoustic waves.

Besides, the time coefficients of a POD mode contain multiple frequencies. For situations such as the jet in crossflow where one is interested in studying the dynamics of low-frequency oscillations, such as wall modes, separate from high-frequency oscillations, such as shear-layer modes, the POD method is not an efficient method to decouple and isolate the dynamics. Thus, it would be helpful if one can invent a frequency based modal decomposition method to identify the dominant frequency from experimental data of fluid flows.

4.3 Literature Review

4.3.1 Proper Orthogonal Decomposition Mode

POD method is a statistical pattern recognition tool used to remove redundant information and thus extract useful information from a large amount of data. POD method was first introduced in turbulence research in [21]. Comprehensive reviews on applications of POD method to turbulence have been done by [22]. In [23, 24], POD is used in developing low-dimensional models of fluids. In [25], the reduce order model for the fixed, high angle of attack flat plate is obtained and compares with direct numerical simulation to show that the reduce order model preserves qualitative behavior such as coherent structures.

4.3.2 Koopman Mode

In [20], a modal decomposition method for nonlinear flows based on spectral analysis of a linear operator, called as Koopman operator defined for any nonlinear system, is presented. Even if the governing dynamics are finite dimensional, the Koopman operator is infinite dimensional and does not rely on the linearization of the dynamics. The Koopman operator captures the full information of nonlinear system. The Koopman modes capture the relevant frequencies more precisely than global eigenmodes of the linearized dynamics, and decouple the different frequency components more efficiently than modes determined by POD.

4.4 Experimental Setup of Flapping Wings

The experimental study was conducted in a closed-circuit low-speed wind tunnel located at the Aerospace Engineering Department of Iowa State University. The tunnel has a test section with a 1.0 $\times$ 1.0 ft (30 $\times$ 30 cm) cross section and the walls of the test section are optically transparent. The tunnel has a contraction section upstream of the test section with honeycombs, screen structures and a cooling system installed ahead of the contraction section to provide uniform low turbulent incoming flow into the test section.

The tested piezoelectric flapping wing has a rectangular platform with the chord length 12.7mm, wingspan 34mm, and thickness 0.26mm.

We use x to denote the horizontal direction and y to denote the vertical direction in this paper. The domain of velocity field measured is: $(x, y) \in [-0.7917, 8.6528] \times [-3.3889, 3.5000]$ inch. The number of grid points of velocity field is 5418 for each snapshot, i.e., 86 grid points in x direction and 63 grid point in y direction. The distance between two grid points for horizontal or vertical direction is 0.1111 inch. At each grid point the velocity components along x and y direction are measured.

In experiment, the flapping frequency of flapping wing microaerial-vehicle is fixed at 60 HZ since the flapping frequency of micro-flapping bird in nature is approximated to 60 HZ. Thus, this experiment is an accurate approximation of the flapping flight of micro-flapping bird in natural environments. While the sampling frequency for non-synchronous data is 3.515556HZ, the sampling frequency for synchronous data (phase lock PIV data) is fixed at 480HZ.

There are two kinds of control inputs, i.e., flapping amplitude and flight speed, in experiment. Based on the type of control inputs, the experimental data are devided into two classes. The first class of data is measured at 50% wingspan of flapping wing for different flapping amplitude, and the second class of data is measured at wingtip for different flight speed. As for the same control input, the synchronous data and non-synchronous data are obtained.

For convenience, we will use 2 shorthands, 50%120v and 50%200v, to denote these two classes of data in the following chapters. 50%120v data means that data is measured at the 50% wingspan for small flapping amplitude (The voltage of motor controlling the flapping amplitude is 120 volt). And 50%200v data means that data is measured at the 50% wingspan for large flapping amplitude (The voltage of motor controlling the flapping amplitude is 200 volt). In addition, experimental data for flight speed at 0.879m/s, 3.653 m/s and 9.551 m/s are measured.

CHAPTER 5. PROPER ORTHOGONAL DECOMPOSITION MODE

In this chapter, we use Proper Orthogonal Decomposition (POD) method to analyze the experimental data (PIV measurements) and hence to identify the coherent structure in the wakes of flapping wings.

When we use snapshots to generate the POD modes, we need to figure out how many snapshots should be used in order to generate the POD mode containing full information in the sense that if we use more snapshots than current number of snapshots, the vortex structures in the dominant POD modes (i.e. POD mode 1, POD mode 2, and POD mode 3) will not change. POD mode 1, POD mode 2, and POD mode 3 are called dominant POD modes since the summuation of kinetic energy in POD mode 1, mode 2 and mode 3 is more than 99% of total kinetic energy contained in all POD modes. Moreover, POD mode 1 contains the largest kinetic energy and the associated eigenvalue is also the largest. Similarly, POD mode 2 contains the second largest kinetic energy and the associated eigenvalue is the second largest, and so on and so forth.

In this chapter, 120 snapshots which ensure that each POD mode contains enough information are utilized to generate POD modes in each case. In each figure of POD mode, we use different color to characterize different vortex. The magnitude of the value of colorbar denotes the curl value of vortex, and the sign of value of colorbar denotes the rotation direction of vortex. The negative value in the colorbar denotes that the rotation direction of vortex is clockwise and the positive value in the colorbar is used to indicate that the vortex is counter-clockwise.

The organization of the chapter is as follows. In section 5.1, we compare POD modes of data for different flight speeds and analyze the eigenvalues of dominant POD modes. In

section 5.2, we compare the POD modes of data for different flapping amplitudes, and analyze eigenvalues of these dominant POD modes.

5.1 POD Mode of Data for Different Flight Speeds

In this section, we show POD modes of non-synchronous data and synchronous data for different flight speeds. All data used in this section are measured at wingtip of the flapping wing.

5.1.1 POD Mode of Non-synchronous Data

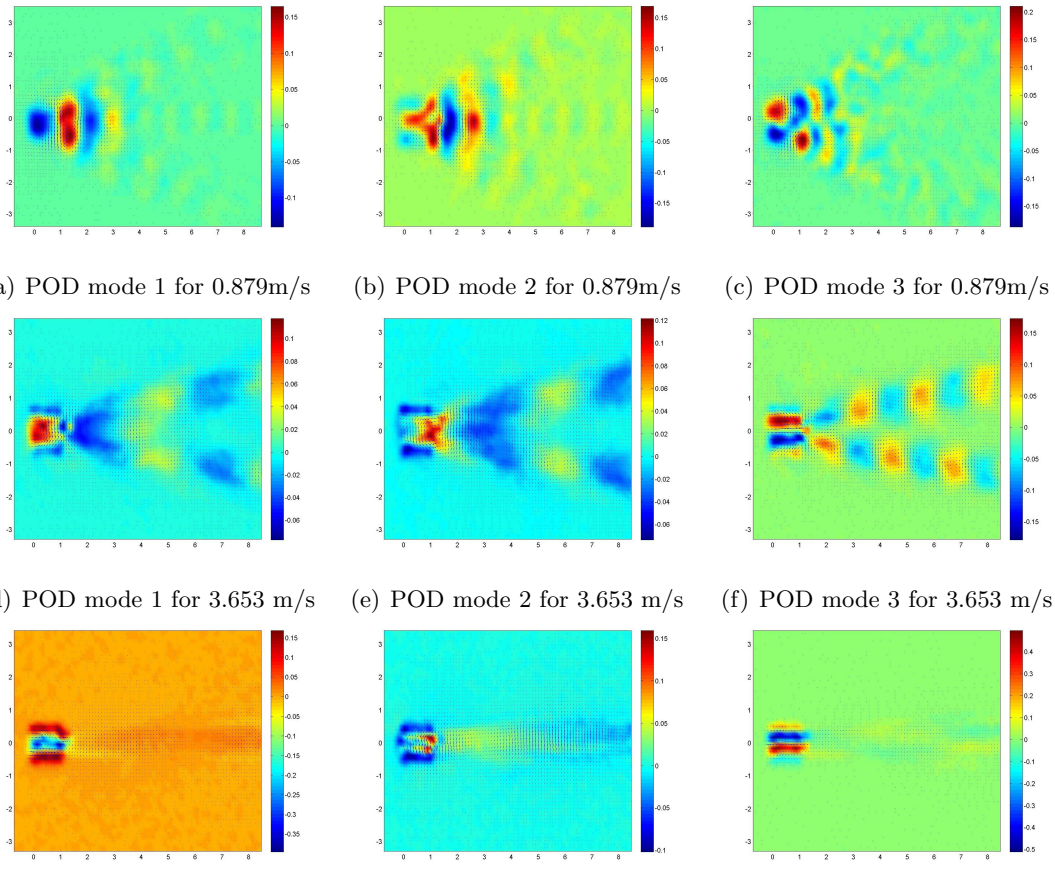

(a) POD mode 1 for 0.879m/s (b) POD mode 2 for 0.879m/s (c) POD mode 3 for 0.879m/s

(d) POD mode 1 for 3.653 m/s (e) POD mode 2 for 3.653 m/s (f) POD mode 3 for 3.653 m/s

(g) POD mode 1 for 9.55098m/s (h) POD mode 2 for 9.55098m/s (i) POD mode 3 for 9.55098m/s

Figure 5.1 POD modes of non-synchronous data for different flight speeds

In Fig. 5.1, we plot POD modes of non-synchronous data for different flight speeds. We can see obvious vortex shedding exists from POD mode 1 to POD mode 3 in each case. Moreover, the turbulence in corresponding POD modes drastically decrease in the wakes flow with the increase in flight speed. For example, the turbulence in subfigure (a) is stronger than the turbulence in subfigure (g). Especially, there almost only exists laminar flow in the wakes of flapping wing in subfigure (g).

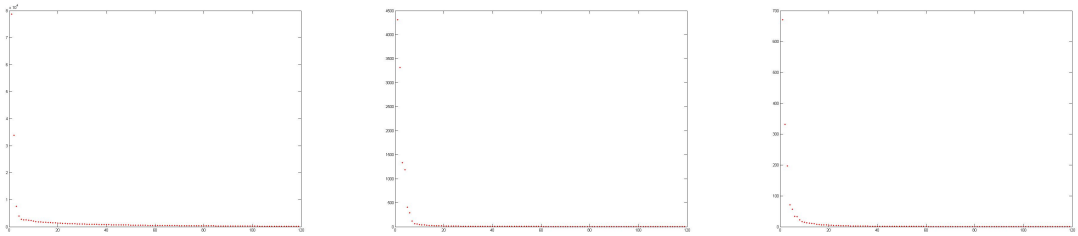

(a) 0.879 m/s (b) 3.653m/s (c) 9.55098 m/s

Figure 5.2 Eigenvalues of POD modes of non-synchronous data for different flight speeds

It is interesting to compare the eigenvalues of dominant POD modes generated from non-synchronous data for different flight speeds since eigenvalue of POD mode equals the kinetic energy contained in each POD mode. In Fig. 5.2, we plot eigenvalues of all POD modes of non-synchronous data for different flight speeds. The largest eigenvalues in subfigure (a), (b), and (c) are equal to 79000, 4400, and 685, respectively. Thus, the eigenvalue of POD mode 1 generated from non-synchronous data decreases with the increase in flight speed of flapping wing. Besides, the second and third largest eigenvalue also decrease with the increase in flight speed of flapping wing.

5.1.2 POD Mode of Synchronous Data

In Fig. 5.3, we plot the POD modes of synchronous data for different flight speeds. In each set of POD modes, vortex shedding occurs naturally. As the flight speed increases, the turbulence in the wakes of flapping wing decreases distinctly in dominant POD modes.

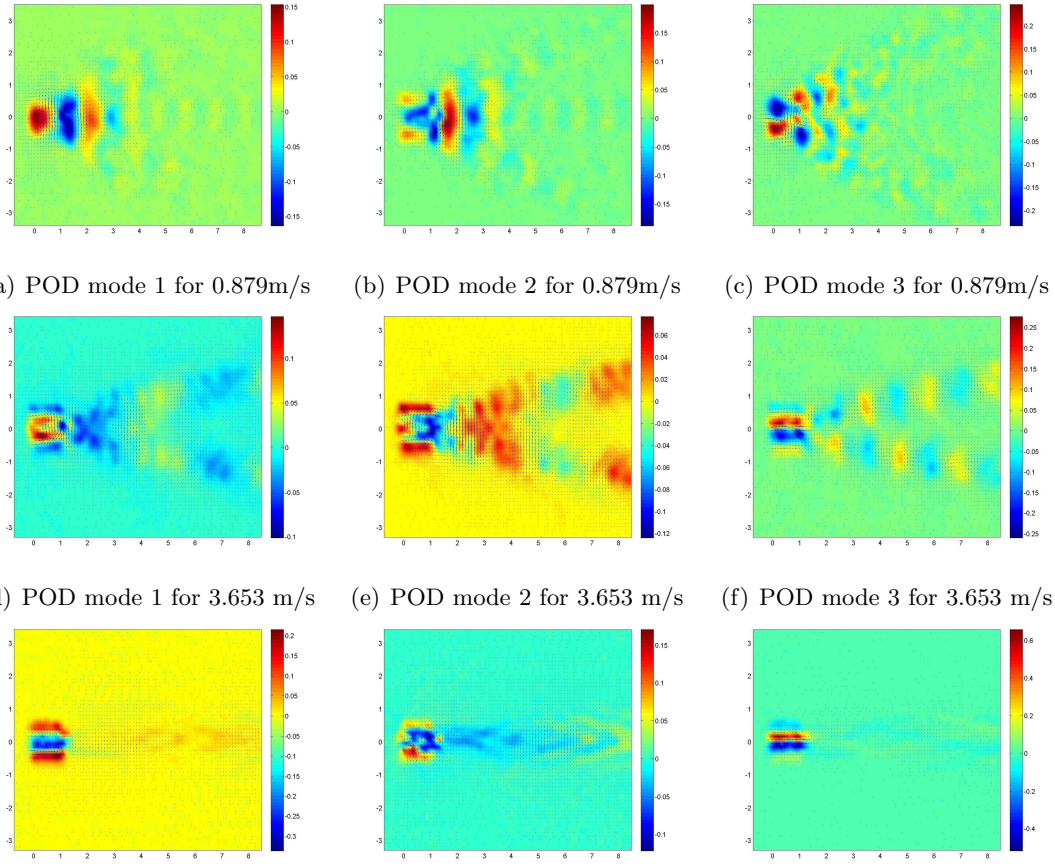

(a) POD mode 1 for 0.879m/s (b) POD mode 2 for 0.879m/s (c) POD mode 3 for 0.879m/s

(d) POD mode 1 for 3.653 m/s (e) POD mode 2 for 3.653 m/s (f) POD mode 3 for 3.653 m/s

(g) POD mode 1 for 9.55098m/s (h) POD mode 2 for 9.55098m/s (i) POD mode 3 for 9.55098m/s

Figure 5.3 POD modes of synchronous data for different flight speeds

Moreover, comparing the corresponding modes in Fig. 5.1 and Fig. 5.3, we can see the corresponding two modes have the same number of dominant vortices associated with the largest curl values, and the dominant vortices occur in the same location of velocity field. For example, there exist 3 dominant vortices structures in subfigure (a) of Fig. 5.1 and Fig. 5.3. The location of corresponding dominant vortices is the same. And the vortex structures of corresponding dominant vortices are very similar.

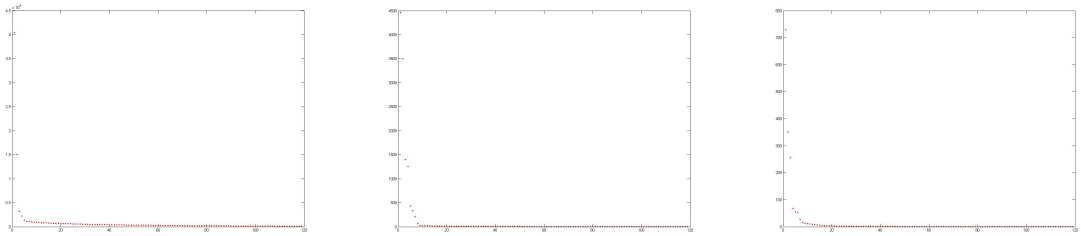

(a) 0.879 m/s (b) 3.653m/s (c) 9.55098 m/s

Figure 5.4 Eigenvalues of POD modes of synchronous data for different flight speeds

In Fig. 5.4, we plot eigenvalues of POD modes generated from synchronous data for different flight speeds. The eigenvalues of POD mode 1 are 41000, 4490, and 720 in subfigure (a), (b), and (c), respectively. Thus, the largest eigenvalue decreases with the increase in flight speed, and the second and third largest eigenvalues also decrease with the increase in flight speed.

Comparing the corresponding subfigures in Fig. 5.2 and Fig. 5.4, the eigenvalues of corresponding dominant POD modes are different. Nevertheless, the magnitudes of corresponding eigenvalues are the same. For example, the eigenvalue of POD mode 1 of non-synchronous data for flight speed 3.653m/s is 4400, and the eigenvalue of POD mode 1 of synchronous data for flight speed 3.653m/s is 4490.

By far, we know using synchronous data and non-synchronous data for the same flight speed will generate similar dominant POD modes because it can be observed that the corresponding dominant POD modes have very similar vortex structures and their associated dominant eigenvalues have the same magnitude.

5.2 POD Mode of Data for Different Flapping Amplitudes

In this section, POD modes of non-synchronous data and synchronous data for different flapping amplitudes are compared. All data used in this section are measured at the 50% wingspan of the flapping wing.

5.2.1 POD Mode of Non-synchronous Data

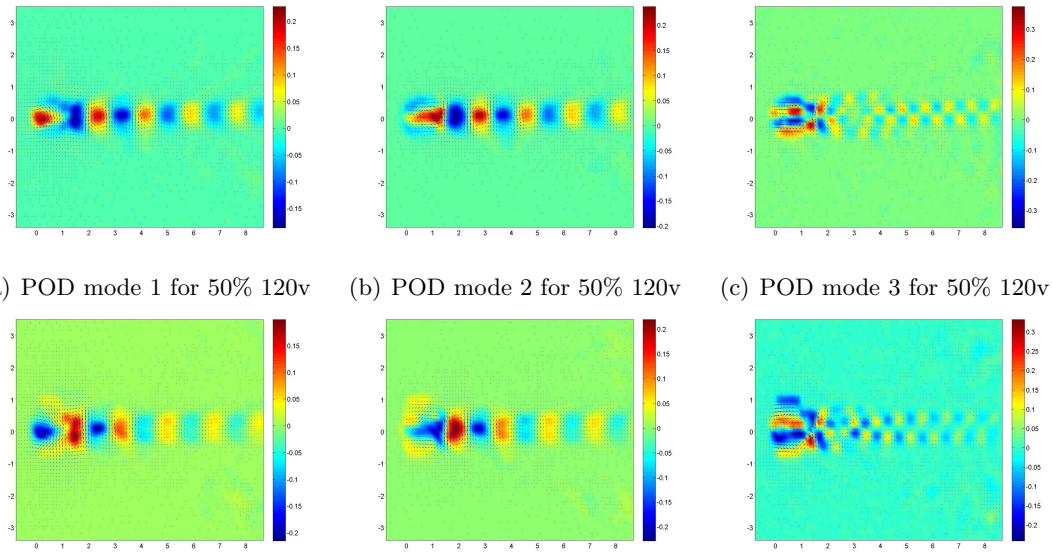

(a) POD mode 1 for 50% 120v (b) POD mode 2 for 50% 120v (c) POD mode 3 for 50% 120v

(d) POD mode 1 for 50% 200v (e) POD mode 2 for 50% 200v (f) POD mode 3 for 50% 200v

Figure 5.5 POD modes of non-synchronous data for different flapping amplitudes

In Fig. 5.5, we plot the POD modes of non-synchronous data for different flapping amplitudes. Apparently, wake turbulence is not affected by the change of flapping amplitude as opposed to the case of POD modes in Fig. 5.1.

Besides, these corresponding POD modes generated from non-synchronous data for different flapping amplitudes are very similar. For example, the vortex structure in Fig. 5.5 (a) and (d) are highly similar except the possible opposite rotation directions for corresponding dominant vortices.

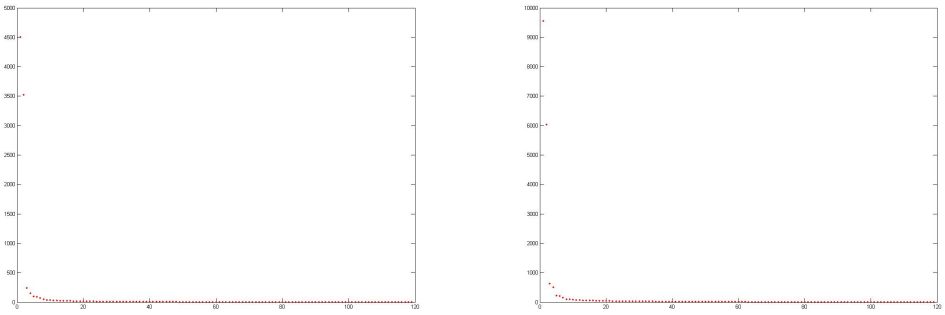

(a) 50% 120v (b) 50% 200v

Figure 5.6 Eigenvalues of POD modes of non-synchronous data for different flapping amplitudes

In Fig. 5.6, we show eigenvalues of POD modes of non-synchronous data for different flapping amplitudes. The eigenvalue of POD mode 1 for small flapping amplitude is 4500 and the eigenvalue for large flapping amplitude is 9600. Thus, for the non-synchronous data for different flapping amplitudes, the eigenvalue for POD mode 1 increases with the increase in flapping amplitude. In addition, the eigenvalues of POD mode 2 and mode 3 of non-synchronous data also increase with the increase in flapping amplitude.

5.2.2 POD Mode of Synchronous Data

In Fig. 5.7, we plot POD modes of synchronous data for different flapping amplitudes. These corresponding dominant POD modes are quite similar. For example, the corresponding vortex structures in POD mode 1 in subfigure (a) and (d) of Fig. 5.7 are absolutely similar except opposite rotation directions of corresponding vortices.

Moreover, comparing the corresponding modes in Fig. 5.5 and Fig. 5.7, we can observe the corresponding two modes have the same number of dominant vortices which occur in the same location.

In Fig. 5.8, we show the eigenvalues of POD modes of synchronous data for different flapping amplitudes. The eigenvalue of POD mode 1 for a small flapping amplitude is 4700 and the

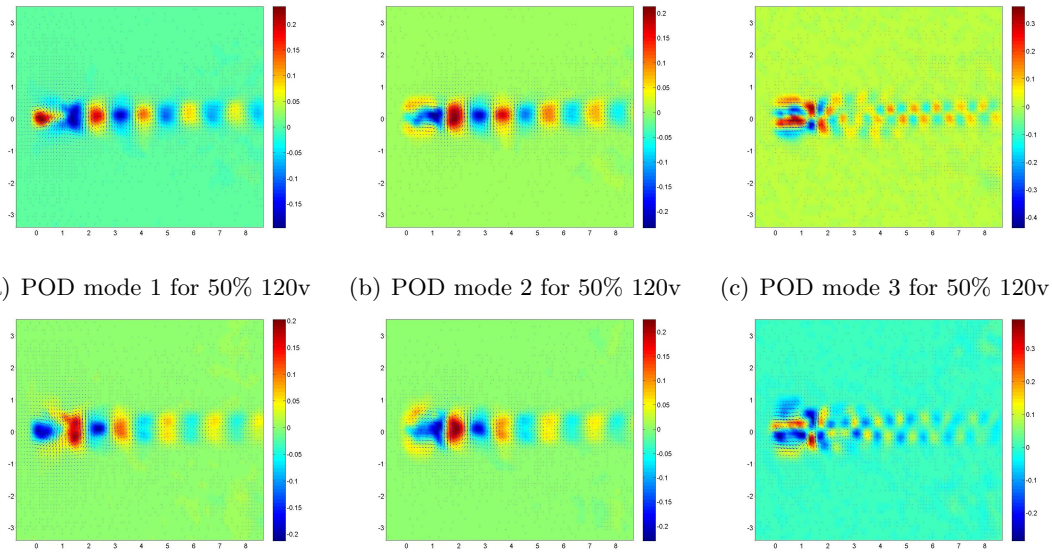

(a) POD mode 1 for 50% 120v (b) POD mode 2 for 50% 120v (c) POD mode 3 for 50% 120v

(d) POD mode 1 for 50% 200v (e) POD mode 2 for 50% 200v (f) POD mode 3 for 50% 200v

Figure 5.7 POD modes of synchronous data for different flapping amplitudes

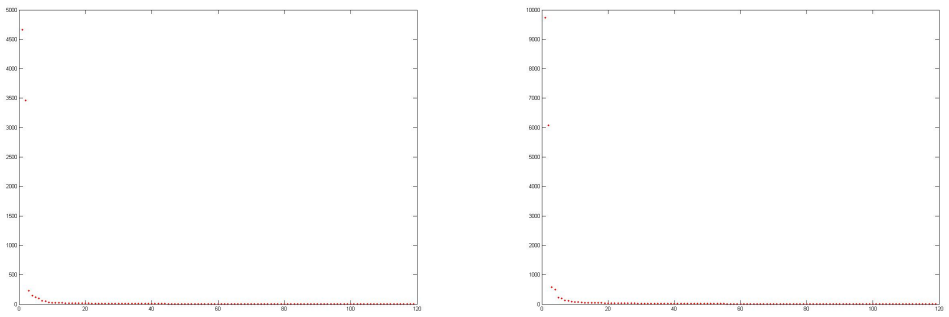

(a) 50% 120v (b) 50% 200v

Figure 5.8 Eigenvalues of POD modes of synchronous data for different flapping amplitudes

eigenvalue of POD mode 1 for a large flapping amplitude is 9800. Thus, for these data, the eigenvalue of POD mode 1 increases with the increase in flapping amplitude. In addition, the eigenvalues of POD mode 2 and mode 3 are also increase with the increase in flapping amplitude. In brief, the eigenvalues of dominant POD modes of synchronous data increase with the increase in flapping amplitude.

Comparing Fig. 5.6 with Fig. 5.8, we observe that although eigenvalues of corresponding dominant POD modes of synchronous and non-synchronous data are different, their magnitudes are the same.

Therefore, we can either use synchronous data or non-synchronous experimental data for the same flapping amplitude to generate the POD modes due to the fact that the corresponding dominant POD modes have quite similar vortex structures and their associated dominant eigenvalues have the same magnitude.

CHAPTER 6. PERRON-FROBENIUS MODE

In this chapter, a new method based on the spectral analysis of the linear transfer operator, called Perron-Frobenius (P-F) operator, associated with any nonlinear flows, is presented.

The organization of the chapter is as follows. In section 6.1, we introduce P-F operator and P-F mode. In section 6.2, an algorithm to generate P-F mode from snapshots of nonlinear fluid flow is presented. In section 6.3, we show the P-F modes of experimental data and then identify the dominant frequency via spectral analysis of P-F modes.

6.1 P-F Operator and P-F Mode

Consider a dynamical system

$$x_{k+1} = f(x_k), \quad \text{where } f \text{ is invertible and } x_k \in \mathbb{R}^n \tag{6.1}$$

From [19], we have following theorem:

Theorem 20. (Perron-Frobenius operator) *Let (X, A, μ) be a measure space, $f : X \to X$ an invertible nonsingular transformation (f^{-1} nonsingular) and P the associated Perron-Frobenius operator. Then for every $\varphi_j \in L^1$,*

$$P\varphi_j(x_k) = \varphi_j(f^{-1}(x_k)) \cdot \left| \frac{df^{-1}(x_k)}{dx_k} \right| \tag{6.2}$$

The principle is to analyze the flow dynamics governed by Equ. 6.1 only from available data using the eigenfunctions and eigenvalues of P-F operator. To this end, let λ_j be the eigenvalue of P-F operator P, and $\varphi_j(x)$ be the eigenfunction of P corresponding to λ_j,

$$P\varphi_j(x) = \lambda_j \varphi_j(x) \quad \text{for} \quad \text{j} = 1, 2, \cdots \tag{6.3}$$

By iteration to above equation,

$$P^k\varphi_j(x) = \lambda_j^k\varphi_j(x) \tag{6.4}$$

Besides, we consider a vector-valued observable $g : \mathbb{R}^n \to \mathbb{R}^n$ where n is the number of states and n is a large number. Hence, $x_k \in \mathbb{R}^n$ contains full information about a flow field at a particular time, $g(x)$ is a vector of any quantities of interest, such as a velocity measurements at various grid points in the flow.

Thus for the k^{th} vector x_k,

$$P^k\varphi_j(x_k) = \lambda_j^k\varphi_j(x_k) \tag{6.5}$$

We expect to expand the vector-valued $g(x)$ in terms of these eigenfunctions by

$$g(x) = \sum_{j=1}^{\infty}\varphi_j(x)v_j \tag{6.6}$$

where, $\varphi_j(x)$ is the P-F eigenfunction and v_j is the P-F mode.

Since the transform $f(x)$ is volume preserving, we can get

$$\left|\frac{df^{-1}(x_k)}{dx_k}\right| = 1 \tag{6.7}$$

According to Equ.(6.1), Equ.(6.2) and Equ.(6.7), one can obtain

$$P\varphi_j(x_k) = \varphi_j(f^{-1}(x_k)) = \varphi_j(x_{k-1}) \tag{6.8}$$

By iteration to above equation,

$$P^k\varphi_j(x_k) = \varphi_j(x_0) \tag{6.9}$$

From Equ.(6.5) and Equ.(6.9) one know

$$P^k\varphi_j(x_k) = \varphi_j(x_0) = \lambda_j^k\varphi_j(x_k) \tag{6.10}$$

$$\varphi_j(x_k) = (\frac{1}{\lambda_j})^k\varphi_j(x_0) \quad \text{for} \quad \lambda_j \neq 0 \tag{6.11}$$

Therefore,

$$g(x_k) = \sum_{j=1}^{\infty}\varphi_j(x_k)v_j = \sum_{j=1}^{\infty}\varphi_j(x_0)(\frac{1}{\lambda_j})^k v_j \tag{6.12}$$

The observable $g(x)$ is a linear combination of P-F modes and the coefficients are the eigenfunctions of P-F operator. $\frac{1}{\lambda_j}$, where λ_j is the eigenvalue of P-F operator, characterizes the temporal behavior of the corresponding P-F mode v_j.

6.2 Algorithm for Generation of P-F Mode from Snapshots

Here, we present the Arnoldi algorithm to compute the P-F modes defined in previous section given only values of a particular snapshots. We will show that the Arnoldi algorithm actually produces approximations to eigenvalues of the P-F operator when applied to a non-linear system. First of all, let us assume that one has a linear dynamical system

$$X_k = BX_{k-1} \tag{6.13}$$

where, $B \in \mathbb{R}^{n\times n}$ is invertible, i.e., $X_{k-1} = B^{-1}X_k$, and n is so large that we can not compute eigenvalues of B directly.

Similar to the approach mentioned in [20], we use the Krylov method, in which one starts with an initial vector X_0 and computes iterates of X_0, to compute the estimations of these eigenvalues. After $m-1$ iterations ($m << n$), one has a collection of m vectors that span a Krylov subspace, given by span$\{X_0, BX_0, B^2X_0, \cdots, B^{m-1}X_0\}$. One can find the approximated eigenvalues and eigenvectors by projecting B onto this m-dimensional subspace, and computing eigenvalues and eigenvectors of the resulting low-rank operator.

We denote the sequence of snapshots by $\{X_0, X_1, \cdots, X_m\}$, where $X_0 = x(t_0)$, $X_1 = x(t_0+\Delta_T)$, $X_2 = x(t_0+2\Delta_T), \cdots$, $X_m = x(t_0+m\Delta_T)$, Δ_T is the sampling period and t_0 is the initial instance to sample data. On the other hand, we define the reverse order snapshots by

$$\{Y_0, Y_1, \cdots, Y_m\} = \{X_m, X_{m-1}, \cdots, X_0\},$$

where, $Y_i = X_{m-i}$ for $i = 0, 1, 2, \cdots, m$.

If we stack the reverse order snapshots into a $n \times m$ Krylov matrix

$$\begin{aligned} K &= [Y_0, Y_1, Y_2, \cdots, Y_{m-1}] \\ &= [X_m, X_{m-1}, X_{m-2}, \cdots, X_1] \\ &= [Y_0, (B^{-1})Y_0, (B^{-1})^2Y_0, \cdots, (B^{-1})^{m-1}Y_0] \end{aligned} \tag{6.14}$$

Then,

$$\begin{aligned}(B^{-1})K &= [B^{-1}Y_0, (B^{-1})^2Y_0, (B^{-1})^3Y_0, \cdots, (B^{-1})^mY_0] \\ &= [Y_1, Y_2, Y_3, \cdots, Y_m] \\ &= KC \end{aligned} \tag{6.15}$$

where, column vector $c = (c_{m-1}, c_{m-2}, c_{m-3}, \cdots, c_0)^T$ and matrix C is given by

$$C = \begin{bmatrix} 0 & 0 & \cdots & 0 & c_{m-1} \\ 1 & 0 & \cdots & 0 & c_{m-2} \\ 0 & 1 & \cdots & 0 & c_{m-3} \\ \vdots & \vdots & \ddots & \vdots & \vdots \\ 0 & 0 & \cdots & 1 & c_0 \end{bmatrix} \tag{6.16}$$

For more general case, the snapshots do not come from linear system. That means we can not assume that the m^{th} iteration is a linear combination of previous iteration. If so, we have a residual r between the actual snapshot Y_m and estimated value $Y_m = c_0Y_0 + c_1Y_1 + c_2Y_2 + \cdots + c_{m-1}Y_{m-1}$ given by Equ.(6.15). The residual r is defined by

$$r = Y_m - Kc = Y_m - \sum_{j=0}^{m-1} c_jY_j \tag{6.17}$$

The residual is minimized when r is orthogonal to span$\{Y_0, Y_1, \cdots, Y_{m-1}\}$.

In addition, let β_i be the eigenvalues of C and a_i be the corresponding eigenvector. Thus,

$$\begin{aligned} Ca_i &= \beta_i a_i \\ (B^{-1})(Ka_i) &= \beta_i(Ka_i) \quad \text{since} \quad K(Ca_i) = (KC)a_i = (B^{-1}K)a_i \end{aligned} \tag{6.18}$$

The eigenvalues of C constitute a subset of eigenvalues of B^{-1} and the eigenvector corresponding to β_i for B^{-1} is $v_i = Ka_i$.

By far, we have converted the problem of computing the eigenvalues of matrix $B^{-1} \in \mathbb{R}^{n\times n}$ whose dimension n is so large that we can not directly compute its eigenvalues and eigenvectors to a more easier problem of computing the eigenvalues and eigenvectors of matrix $C \in \mathbb{R}^{m\times m}$, where $m << n$.

Although above proof is based on linear system, we can also apply this algorithm to non-linear system since we have assumed that the residual r exists between the actual observable X_m and the estimated value $Kc = \sum_{j=0}^{m-1} c_j Y_j$. What's more, the residual r is minimized and it is the best one that we can do according to the projection theorem.

Hereby, the algorithm to compute the P-F modes from snapshots is:

1 Define Krylov matrix K by Equ. (6.14) and find constant vector c such that

$$r = Y_m - Kc = Y_m - \sum_{j=0}^{m-1} c_j Y_j, \quad r \perp \text{ span}\{Y_0, Y_1, \cdots, Y_{m-1}\}$$

2 Define matrix C by Equ.(6.16) and find its eigenvalue λ_i and eigenvector a_i. The frequency f_j corresponding to λ_j can be obtained by following equation:

$$f_j = \frac{Im\{log\lambda_j\}}{2\pi\Delta_T} \tag{6.19}$$

where, Δ_T is the sampling period.

3 Define $v_i = Ka_i$ where v_i is the i^{th} P-F mode.

Since P-F operator is a unitary operator and we use finite dimension approximation of the infinite dimensional linear P-F operator that best describes the time evolution of the snapshots data, eigenvalues of P-F modes locate on the unit circle on the complex plane. That is, multiple eigenvalues are 1 and all other eigenvalues are complex conjugates pair whose absolute value is equal to 1.

6.3 P-F Mode and Dominant Frequency of Experimental Data

In this section, we will show the P-F modes generated from different experimental data. 120 snapshots are used to generate P-F modes in each case. The P-F mode 0 denoting the mean flow and having the eigenvalue 1 has frequency 0 by Equation (6.19). Since the eigenvalues associated with P-F mode 2 and P-F mode 3 are complex conjugate leading that the absolute value of P-F mode 2 and P-F mode 3 are the same, we only show P-F mode 1, mode 2, and mode 4 in this section.

In each figure of P-F mode, we use different colors to characterize different vortices. The magnitude in colorbar denotes curl value of vortex, and sign of colorbar denotes rotation direction of vortex. The negative value in colorbar denotes that the rotation direction of vortex is clockwise and the positive value indicates that the vortex has a counter-clockwise rotation direction.

6.3.1 P-F Mode and Dominant Frequency of Data for Different Flight Speeds

In this section, we show the P-F modes of non-synchronous data and synchronous data for different flight speeds of flapping wing. Then we identify the dominant frequency of experimental data via spectral analysis of P-F modes. The data used in this section are measured at the wingtip of the flapping wing.

6.3.1.1 P-F Mode of Non-synchronous Data for Different Flight Speeds

In Fig. 6.1, we plot the P-F modes of non-synchronous data for different flight speeds. It shows that with the increase in flight speed, turbulence in the wake flows becomes increasingly vague for corresponding P-F modes. If the flight speed equals to 0.879m/s, vortex shedding is unavoidable and the flow behind the trailing of flapping wing is turbulent. As the flight speed increases to 9.55098 m/s, vortex shedding does not occur in the wakes and almost all flows are laminar flows behind the trailing of the flapping wing.

6.3.1.2 Dominant Frequency of Non-synchronous Data for Different Flight Speeds

In Fig. 6.2, each subfigure shows the magnitudes of all P-F modes (except the P-F mode 0) of non-synchronous data at each frequency. Since the spectrum is symmetrical with respect to the y axis (normalized magnitude), only positive frequencies in the x axis are plotted. In each subfigure, the dominant frequency corresponding to magnitude 1 is close to 0.25 HZ.

In order to understand the significance of 0.25 HZ determined by P-F method, we use the Fast Fourier Transformation (FFT) to analyze the velocity data recorded at the fixed point

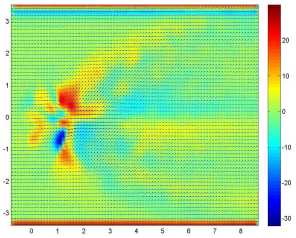

(a) P-F mode 1 for 0.879m/s

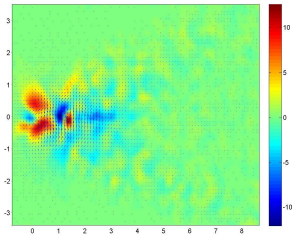

(b) P-F mode 2 for 0.879m/s

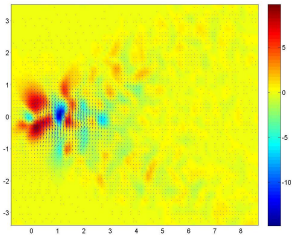

(c) P-F mode 4 for 0.879m/s

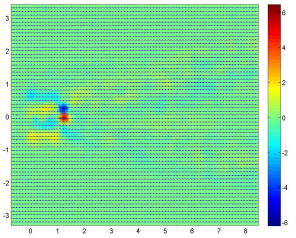

(d) P-F mode 1 for 3.653 m/s

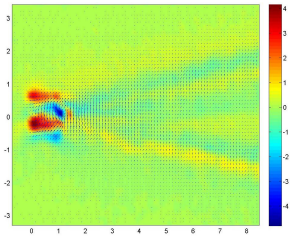

(e) P-F mode 2 for 3.653 m/s

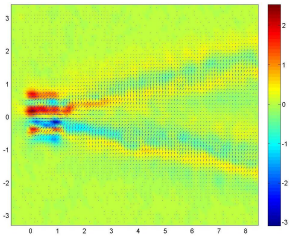

(f) P-F mode 4 for 3.653 m/s

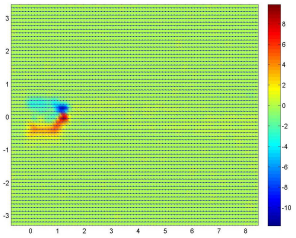

(g) P-F mode 1 for 9.55098m/s

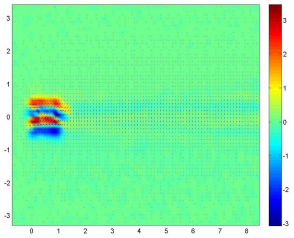

(h) P-F mode 2 for 9.55098m/s

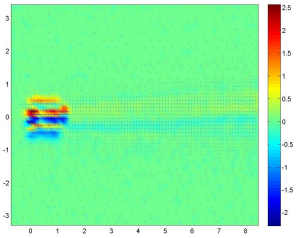

(i) P-F mode 4 for 9.55098m/s

Figure 6.1 P-F modes of non-synchronous data for different flight speeds

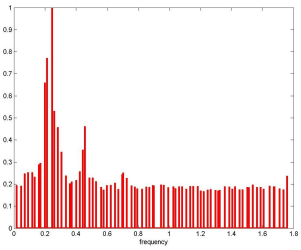

(a) 0.879m/s

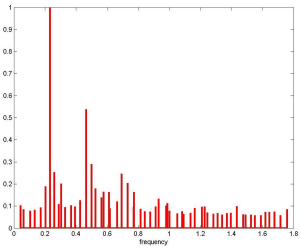

(b) 3.653 m/s

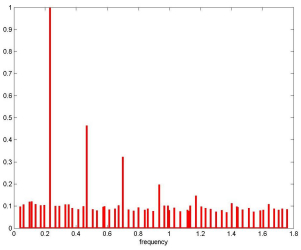

(c) 9.55098m/s

Figure 6.2 Frequencies of P-F modes of non-synchronous data for different flight speeds

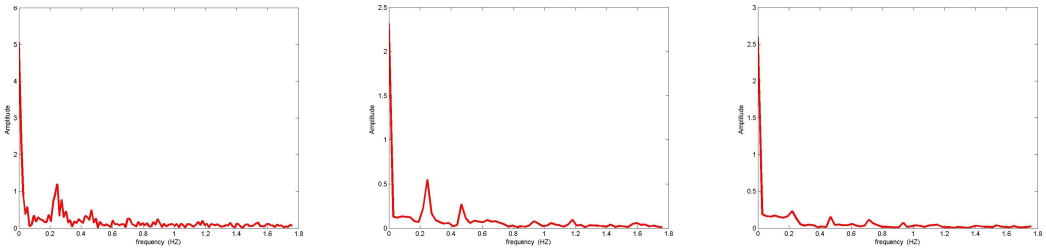

(a) 0.879m/s (b) 3.653 m/s (c) 9.55098m/s

Figure 6.3 Frequencies of non-synchronous data for different flight speed

with coordinate $(0.0972, -0.5)$ where dominant vortex occurs from observation. The dominant frequency of the vector field over the whole space can be identified by FFT of the velocity data.

We can observe the dominant frequency in each subfigure of Fig. 6.3 is closed to 0.25 HZ, which is the frequency identified by spectral analysis of P-F modes. Thus, it verifies that the spectrum of P-F modes can identify the dominant frequency of nonlinear flows. Besides, it shows that the dominant frequency of non-synchronous data for different flight speeds is not sensitive to the change of the flight speed and is almost constant, 0.25 HZ.

6.3.1.3 P-F Mode of Synchronous Data for Different Flight Speeds

In Fig. 6.4, we plot the P-F modes of synchronous data for different flight speeds. The turbulence in the wakes becomes increasingly vague with the increase in flight speed. If the flight speed increases to 9.55098m/s, the fluid flows behind the trailing of flapping wing almost become laminar.

6.3.1.4 Dominant Frequency of Synchronous Data for Different Flight Speeds

In Fig. 6.5, we plot magnitudes of the P-F modes (except the P-F mode 0) of synchronous data for different flight speeds at each frequency. The dominant frequency is approximated to 60 HZ. As we know, 60 HZ is in fact the flapping frequency of flapping wing. This means we can use the P-F method to identify the flapping frequency from the synchronous data of

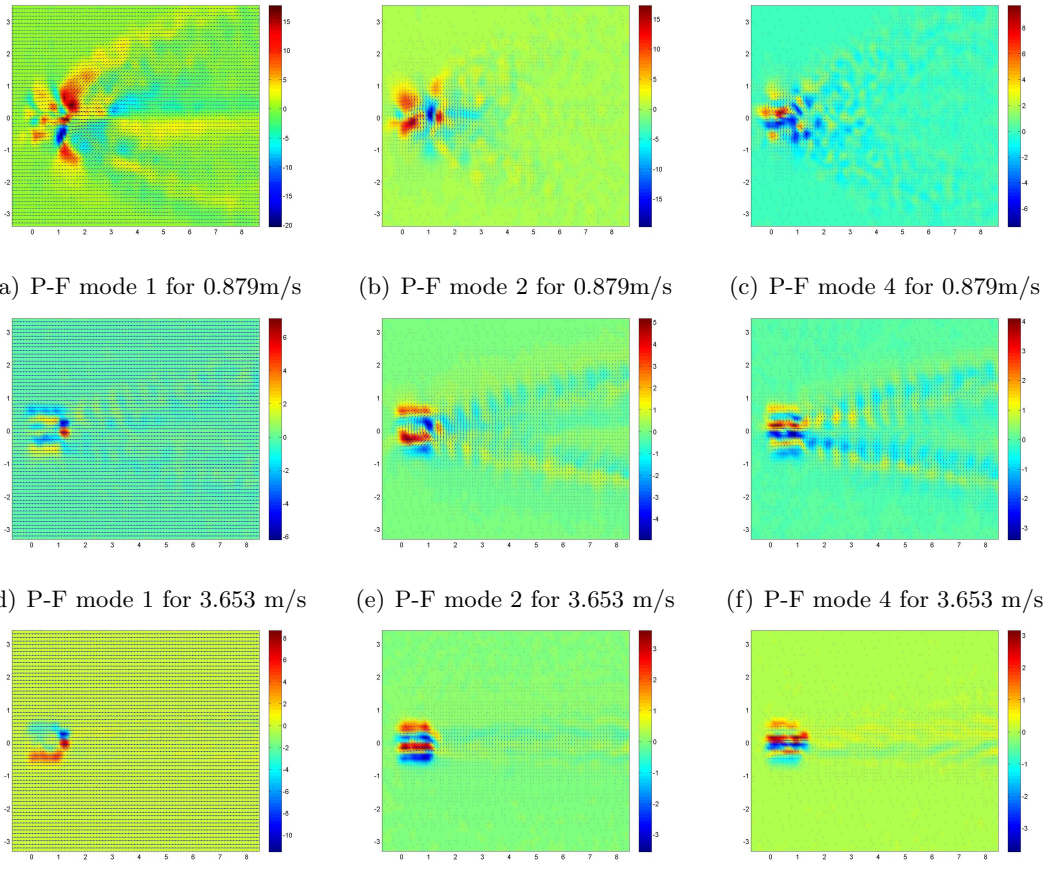

(a) P-F mode 1 for 0.879m/s (b) P-F mode 2 for 0.879m/s (c) P-F mode 4 for 0.879m/s

(d) P-F mode 1 for 3.653 m/s (e) P-F mode 2 for 3.653 m/s (f) P-F mode 4 for 3.653 m/s

(g) P-F mode 1 for 9.55098m/s (h) P-F mode 2 for 9.55098m/s (i) P-F mode 4 for 9.55098m/s

Figure 6.4 P-F modes of synchronous data for different flight speeds

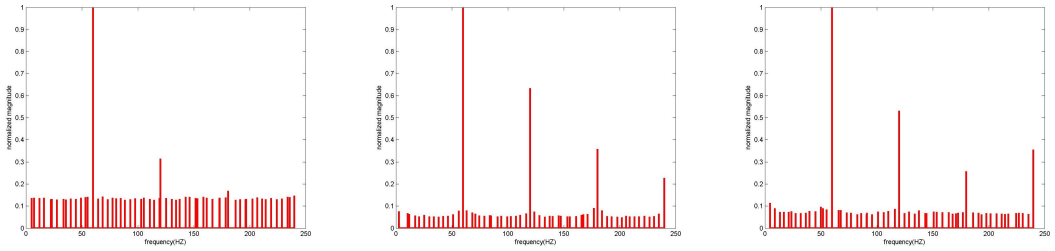

(a) 0.879m/s (b) 3.653 m/s (c) 9.55098m/s

Figure 6.5 Frequencies of P-F modes of synchronous data for different flight speeds

flapping wing.

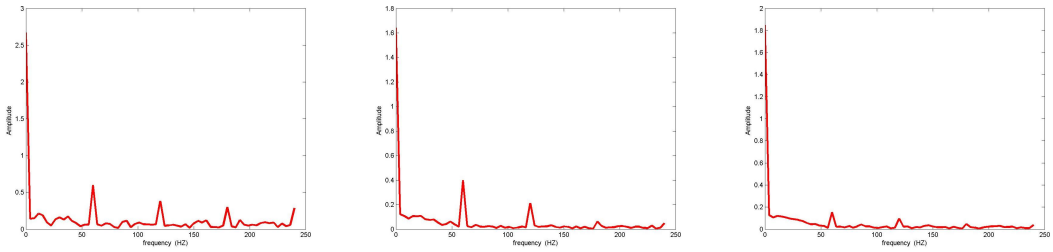

(a) 0.879m/s (b) 3.653 m/s (c) 9.55098m/s

Figure 6.6 Frequencies of synchronous data for different flight speeds

Once more, we use FFT to check if the spectral analysis of P-F operator determines the dominant frequency of fluid flow. In Fig. 6.6, the dominant frequency of synchronous data in each subfigure is equal to 60 HZ according to the FFT of the velocity data recorded at the point $(0.0972, -0.5)$ where dominant vortex occurs. It verifies that the dominant frequency obtained from the P-F method is correct.

6.3.2 P-F Mode and Dominant Frequency of Data for Different Flapping Amplitudes

In this section, we show the P-F modes of non-synchronous data and synchronous data for different flapping amplitudes of flapping wing. Moreover, we utilize the spectral analysis of P-F modes to identify the dominant frequency of experimental data. All data used in this section are measured at 50% wingspan of the flapping wing.

6.3.2.1 P-F Mode of Non-synchronous Data for Different Flapping Amplitude

In Fig. 6.7, we plot the P-F modes of non-synchronous data for different flapping amplitudes. It shows that the vortex shedding in the wakes is not evidently affected with the increase in flapping amplitude.

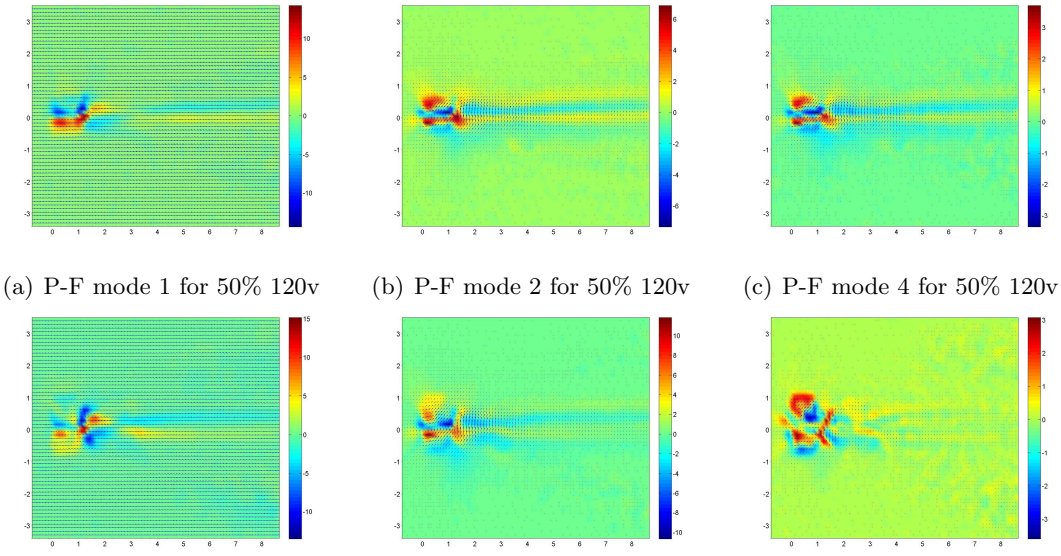

(a) P-F mode 1 for 50% 120v (b) P-F mode 2 for 50% 120v (c) P-F mode 4 for 50% 120v

(d) P-F mode 1 for 50% 200v (e) P-F mode 2 for 50% 200v (f) P-F mode 4 for 50% 200v

Figure 6.7 P-F modes of non-synchronous data for different flapping amplitudes

6.3.2.2 Dominant Frequency of Non-synchronous Data for Different Flapping Amplitudes

In Fig. 6.8, we plot magnitudes of the P-F modes (except the P-F mode 0) of non-synchronous data for different flight speeds at each frequency. The dominant frequency is approximated to 0.25 HZ in each subfigure.

Again, we use FFT to analyze a velocity data by recording velocities at the fixed point $(0.0972, -0.5)$ where dominant vortex occurs. In Fig. 6.9, we find the dominant frequency is closed to 0.25 HZ in each subfigure verifying that P-F modes based method can identify the dominant frequency of nonlinear flows.

6.3.2.3 P-F Mode of Synchronous Data for Different Flapping Amplitudes

In Fig. 6.10, we plot the P-F modes of synchronous data for different flapping amplitudes. It shows the flapping amplitude has a trivial impact on generation of P-F modes.

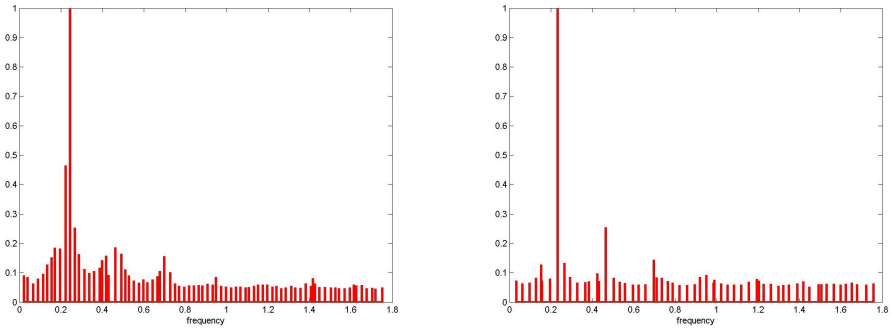

(a) 50% 120v (b) 50% 200v

Figure 6.8 Frequencies of P-F modes of non-synchronous data for different flapping amplitudes

6.3.2.4 Dominant Frequency of Synchronous Data for Different Flapping Amplitudes

In Fig. 6.11, we plot the frequencies of synchronous data for different flapping amplitudes. The dominant frequency is approximated to 60 HZ in each subfigure which is the flapping frequency of flapping wing.

Once again, we show the frequencies of synchronous data for different flapping amplitudes in Fig. 6.12 by FFT analysis of the velocity data at point with coordinate $(0.0972, -0.5)$ where dominant vortex occurs. The dominant frequency is approximated to 60 HZ in each subfigure, which confirms the dominant frequency in Fig. 6.11.

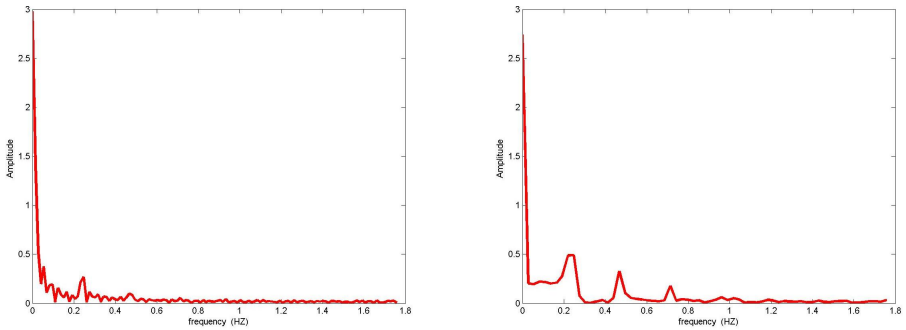

(a) 50% 120v (b) 50% 200v

Figure 6.9 Frequencies of non-synchronous data for different flapping amplitudes

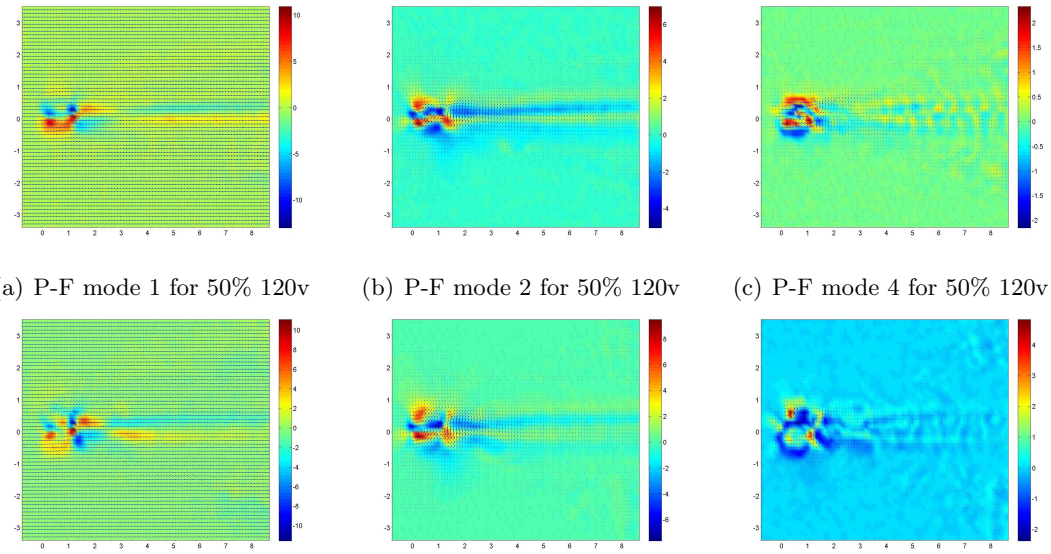

(a) P-F mode 1 for 50% 120v (b) P-F mode 2 for 50% 120v (c) P-F mode 4 for 50% 120v

(d) P-F mode 1 for 50% 200v (e) P-F mode 2 for 50% 200v (f) P-F mode 4 for 50% 200v

Figure 6.10 P-F modes of synchronous data for different flapping amplitudes

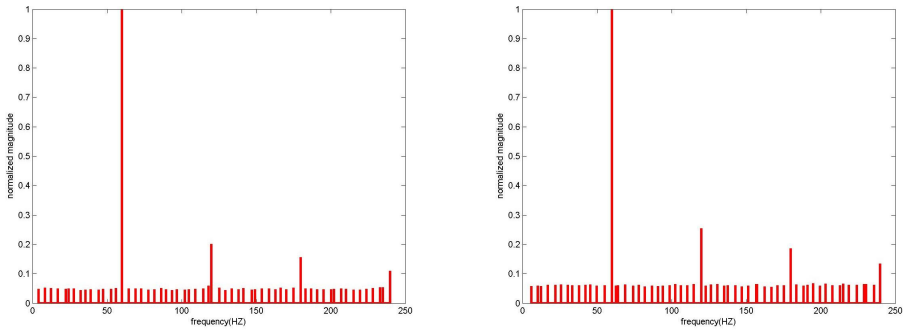

(a) 50% 120v (b) 50% 200v

Figure 6.11 Frequencies of P-F modes of synchronous data for different flapping amplitudes

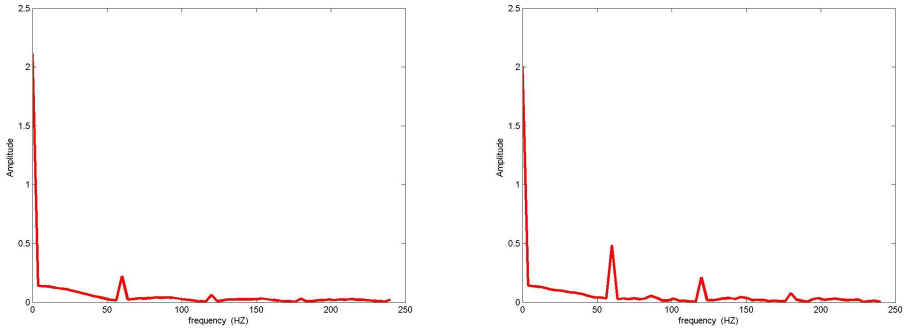

(a) 50% 120v (b) 50% 200v

Figure 6.12 Frequencies of synchronous data for different flapping amplitudes

CHAPTER 7. CONCLUSIONS AND FUTURE RESEARCH

7.1 Conclusions

Experimental data of flapping wing can be used to generate the POD modes which can further be used to identify the vortex structures in the wakes of flapping wing. These POD modes are compared to identify high energy modes that remain invariant across the range of operating conditions.

About vortex structures and kinetic energy analysis based on POD method, we can draw following conclusions: First of all, the corresponding dominant POD modes of synchronous data and non-synchronous data for same control input, i.e., flapping amplitude or flight speed, have very similar vortex structures and their associated dominant eigenvalues have the same magnitude. Secondly, the turbulence in the wakes of flapping wing becomes vague with the increase in flight speed of flapping wing. In contrast, the increase of flapping amplitude will not affect the turbulence in the wakes. Thirdly, while the energy contained in the dominant (high energy) POD modes decreases with the increase in flight speed, the energy contained in the dominant POD mode increases with increase in flapping amplitude.

Contrast to the energy-based POD analysis of vortex structures in the wakes of flapping wings, we present the frequency-based model decomposition method, P-F method, to investigate the dynamical behavior of nonlinear systems and then apply this method to analyze vortex structures in the wakes of flapping wings and characterize the dominant frequency of experimental data.

We show that P-F modes for nonlinear system can be generated by Arnoldi algorithm using the reverse order flow. Furthermore, P-F modes is not only used to analyze the vortex structures but also characterize the dominant frequency of fluid flows. On the one hand, in

vortex structures analysis the turbulence in the wakes becomes vague with the increase in flight speed but it is almost unchanged with the increase in flapping amplitude. This conclusion is consistent with the result of POD analysis in vortex structures. Whereas on the other hand, in dominant frequency analysis the dominant frequency can be extracted from the experimental data by P-F method. Especially, the dominant frequency for synchronous data is in fact the flapping frequency of flapping wing.

Finally, we can draw the conclusion that the integration of energy-based POD method and frequency-based P-F mode method gives a comprehensive understanding of experimental data of flapping wings.

7.2 Future Research

As we know, the POD modes are not only used to analyze the spatial structure of vortex in nonlinear flow but also used to construct the reduced order model of high-dimensional partial differential equation, for example, Naiver Stokes equations. For future research, we expect to get the reduce order model by Galerkin projection of the governing Naiver Stokes equations onto those POD modes generated from experimental data of flapping wing. Then the reduce order model can be compared to the direct numerical simulation of flapping wing to show coherent structure in the reduce order model is preserved.

BIBLIOGRAPHY

[1] M. Dellnitz, G. Froyland, and O. Junge, "The algorithms behind GAIO - Set oriented numerical methods for dynamical systems," in *Ergodic Theory, Analysis, and Efficient Simulation of Dynamical systems*, pp. 145–174, Springer, 2000.

[2] H. K. Khalil, *Nolinear Systems, Thrid Edition.* Prentice Hall, 2001.

[3] G. Chesi, "Domain of attraction: Estimates for non-polynomial systems via LMIs," *Proc. 16th IFAC World Congress on Automatic Control*, 2005.

[4] R. Genesio, M. Tartaglia, and A. Vicino, "On the estimation of asymptotic stability regions: State of the art and new proposals," *IEEE Transactions on Automatic Control*, vol. AC-30, no. 8, pp. 747–755, August 1985.

[5] P. Parrilo, "Semidefinite programming relaxations for semialgebraic problems," *Mathematical Programming Series B*, vol. 96, no. 2, pp. 293–320, 2003.

[6] U. Topcu, A. Packard, and P. Seiler, "Local stability analysis using simulations and sum-of-squares programming," *Automatica*, vol. 44, pp. 2669–2675, 2008.

[7] B. Tibken and Y. Fan, "Computing the domain of attraction for polynomial systems via BMI optimal method," *Proceddings of 2006 American Control Conference*, 2006.

[8] W. Tan and A. Packard, "Stability region analysis using sum of square programming," *Proceddings of 2006 American Control Conference*, 2006.

[9] B. Tibken and O. Hachicho, "Estimation of the domain of attraction for polynomial systems using multidimensional grids," *Proceddings of the 39th IEEE, Conference on Decision and Control*, 2000.

[10] G. Chesi, "Estimating the domain of attraction for non-polynomial systems via LMI optimizations," *Automatica*, vol. 45, pp. 1536–1541, 2009.

[11] U. Vaidya and P. G. Mehta, "Lyapunov measure for almost everywhere stability," *IEEE Transactions on Automatic Control*, vol. 53, no. 1, pp. 307–323, February 2008.

[12] U. Vaidya, "Converse theorem for almost everywhere stability using Lyapunov measure," *Proceedings of the 2007 American Control Conference*, July 11-13, 2007.

[13] U. Vaidya and P. G. Mehta, "Computation of Lyapunov measure for almost everywhere stability," *Proceedings of the 45th IEEE Conference on Decision & Control*, December 13-15, 2006.

[14] B. Fiedler, *Ergodic Theory, Analysis, and Efficient Simulation of Dynamical systems*. Berlin: Springer-Verlag, 2001.

[15] G. Froyland, "Extracting dynamical behaviour via Markov models," in *Proceedings, Newton Institute*, pp. 283–324, Birkhauser.

[16] C. M. Grinstead and J. L. Snell, *Introduction to Probability*. American Mathematical Society, 1997.

[17] J. Pospisil, Z. Kolka, J. Horska, and J. Brobohaty, "Simplest ODE equivalents of Chua's equations," *International Journal of Bifurcation and Chaos*, vol. 10, no. 1, pp. 1–23, 2000.

[18] C. Rowley, "Model reduction for fluids,using balanced proper orthogonal decomposition," *Int. J. on Bifurcation and Chaos*, vol. 15, no. 3, pp. 997–1013, 2005.

[19] A. Lasota and M. C. Mackey, *Chaos, Fractals, and Noise: Stochastic Aspects of Dynamics*. Applied Mathematical Sciences, 1993.

[20] C. W. Rowley, I. Mezic, S. Bagheri, P. Schlatter, and D. Henningson, "Spectral analysis of nonlinear flows," *J. Fluid Mechanics*, vol. 641, pp. 115–127, 2009.

[21] Lumley, "The structure of inhomogeneous turbulence," *Atmospheric turbulence and wave propagation*, pp. 166–178, 1967.

[22] P. Holmes, J. L. Lumley, and G. Berkooz, *Turbulence, Coherent Structures, Dynamical Systems and Symmetry*. Cambridge University Press, 1996.

[23] S. S. Ravindran, "Proper orthogonal decomposition in optimal control of fluids," *Int. J. Numer. Meth. Fluids*, vol. 34, pp. 425–448, 1999.

[24] M. Rathinam and L. R. Petzold, "A new look at proper orthogonal decomposition," *SIAM J. Numer*, vol. 41, no. 5, pp. 1893–1925, 2003.

[25] S. Brunton and C. W. Rowley, "Modeling the unsteady aerodynamic forces on small-scale wings," *47th AIAA Aerospace Sciences Meeting*, January 2009.